

ESD RECORD COPY

RETURN TO
SCIENTIFIC & TECHNICAL INFORMATION DIVISION
(ESTI), BUILDING 1211

ESD ACCESSION LIST

ESTI Call No. **60518**

Copy No. 1 of 2 cys.

ESL

1

172

Solid State Research

1968

Prepared under Electronic Systems Division Contract AF 19(628)-5167 by

Lincoln Laboratory

MASSACHUSETTS INSTITUTE OF TECHNOLOGY

Lexington, Massachusetts



AD6667-762

The work reported in this document was performed at Lincoln Laboratory, a center for research operated by Massachusetts Institute of Technology, with the support of the U.S. Air Force under Contract AF 19(628)-5167.

This report may be reproduced to satisfy needs of U.S. Government agencies.

This document has been approved for public release and sale; its distribution is unlimited.

Non-Lincoln Recipients

PLEASE DO NOT RETURN

Permission is given to destroy this document when it is no longer needed.

1

Solid State Research

1968

Issued 12 April 1968

Lincoln Laboratory

MASSACHUSETTS INSTITUTE OF TECHNOLOGY

Lexington, Massachusetts



ABSTRACT

This report covers in detail the solid state research work at Lincoln Laboratory for the period 1 November 1967 through 31 January 1968. The topics covered are Solid State Device Research, Optical Techniques and Devices, Materials Research, and Physics of Solids.

Accepted for the Air Force
Franklin C. Hudson
Chief, Lincoln Laboratory Office

INTRODUCTION

I. SOLID STATE DEVICE RESEARCH

Type conversion and p-n junctions have been produced in n-type CdTe by implantation of 400 keV arsenic ions. The CdTe samples were pre-annealed in cadmium vapor, in order to insure n-type conductivity, and coated with $\sim 1500 \text{ \AA}$ of SiO_2 so that they could be heated to 500°C during implantation. Following implantation, the SiO_2 was removed and each sample was annealed at 650°C with CdTe powder and cadmium. Hall effect measurements and DC thermal probe tests indicate that the implanted region was converted to p-type while the unimplanted region remained n-type. The diodes between the implanted and unimplanted regions had sharp reverse breakdowns at 40 to 50 volts, forward resistances of 30 ohms, and in forward bias emitted bandgap infrared radiation. Similar experiments using a 400 keV argon ion beam gave no evidence of type conversion.

The volt-ampere characteristics of a number of diodes fabricated from vapor-grown, annealed $\text{Pb}_{1-x}\text{Sn}_x\text{Te}$ have been greatly improved by electrolytic etching. For example, the zero bias impedance of one $\text{Pb}_{0.85}\text{Sn}_{0.15}\text{Te}$ diode was increased from 3 to approximately 2000 ohms at 77°K and to approximately 5000 ohms at 12°K . The present results indicate that the surface condition of $\text{Pb}_{1-x}\text{Sn}_x\text{Te}$ diodes plays an important part in determining the zero-bias impedance and that this impedance can in some devices be increased substantially by suitable surface preparation. This offers the possibility of greatly improving the performance of $\text{Pb}_{1-x}\text{Sn}_x\text{Te}$ photovoltaic detectors and lasers.

The spectral response of an InSb-MOS photovoltaic detector has been studied at 77° , 195° and 300°K in the wavelength region between 2.5 and 0.25μ . A photovoltage developed across the MOS structure is observed at wavelengths between 1.25 and 0.25μ , with a single broad peak at about 0.3μ . Measurements of the response of the MOS detector to near-IR radiation while the detector is being irradiated with light of a different energy indicate that there are long-lived states of the detector which can be changed by irradiating the detector with light of wavelengths less than 1.25μ . We expect to find that this effect is related to the MOS detector response in the infrared and to the photovoltage observed around 0.3μ .

A number of CdS platelets were grown in a flowing hydrogen atmosphere with elemental cadmium and sulfur as source materials. Resistivity and Hall constant measurements at 300°K and 77°K indicate that undoped as-grown CdS platelets with good electrical properties can be obtained using this growth process.

A technique has been developed for etching patterns in silicon nitride layers using a thin layer of silicon as an etch mask. This layer is deposited over the silicon nitride using the same reactor system as was used in depositing the silicon nitride. Patterns are etched in the silicon over-layer using standard photolithographic techniques, and concentrated hydrofluoric or hot phosphoric acid can then be used to remove the exposed areas of silicon nitride. These same steps can be used to etch openings in layered structures of silicon nitride over silicon dioxide. In this case hot phosphoric acid should be used as the etchant for the silicon nitride.

II. OPTICAL TECHNIQUES AND DEVICES

A 9-meter long CO_2 10.6- μm amplifier has been operated at greater than 100 W output power with an input power of only 5 W. The power efficiency was 11.5 percent. The water-cooled tubes utilized a flowing gas mixture, and no appreciable beam (mode) distortion was visually observed using a thermally sensitive detector.

In the preliminary tests of a scaled-up sealed-off laser, single frequency output powers up to 15 W have been obtained. Spectrum analyzer displays of the beat note indicated a short-term frequency stability of the same order of magnitude as previously observed with two 1.5-W tubes.

Background-limited operation of copper-doped germanium detectors has been obtained for a background as low as 10^{-11} W (5×10^8 photon/sec) in the 8- to 12- μ region. A cooled FET circuit permits the measurement of these low backgrounds. Preliminary measurements of response vs temperature indicate two regions of near linear behavior: one region between 4.5° and 7°K and another between 8° and approximately 12°K, with a transition region between 7° and 8°K.

Preliminary experiments have been performed to determine the feasibility of using a pair of semiconductor p-n junction lasers, one of which is "tuned" by a magnetic field, to produce heterodyne IF frequencies extending continuously into the GHz range. Mode spectra of several PbTe units have been obtained, one of which exhibited single-mode CW operation. Also, the stability of the wavelength of coherent emission from a diode laser has been analyzed.

Excess noise and anomalous gain have been observed in Ge:Cu photodetectors at frequencies small compared with the reciprocal carrier lifetime. These are attributed to minority carrier injection at the contacts. In heterodyne operation, amplitude fluctuations of the laser local oscillator are found to be troublesome, even at tens of megahertz.

III. MATERIALS RESEARCH

An open tube reactor has been constructed for synthesizing compounds of volatile elements at essentially constant pressure by repeatedly dropping small amounts of the reaction mixture into a crucible hot enough to produce rapid vaporization and reaction. Use of this apparatus has made it possible to produce such compounds as ZnTe and ZnSe at the rate of 100 to 300 g/h, without the risk of explosions which frequently occur when volatile elements are reacted in closed ampoules.

Forced convection in an open tube has been used for the vapor growth of $\text{Pb}_{1-x}\text{Sn}_x\text{Te}$, $\text{ZnTe}_{1-x}\text{Se}_x$, and Cd_3As_2 single crystals about 1 to 10 mm on a side. Helium and hydrogen were used as carrier gases to obtain vapor transport rates higher than those achieved by diffusion or natural convection in closed systems.

Partial pressures of $\text{Te}_2(\text{g})$ and $\text{SiTe}(\text{g})$ in equilibrium with Si-Te samples containing between 10 and 100 atomic percent Te have been determined by measuring the optical density of the vapor for sample temperatures between 500° and 940°C. The results confirm the existence of $\text{Si}_2\text{Te}_3(\text{c})$ as the only solid compound in the Si-Te system, and yield values for the free energies of formation of $\text{Si}_2\text{Te}_3(\text{c})$ and $\text{SiTe}(\text{g})$.

Introduction

The high-pressure phase diagram of InSb has been further investigated by means of superconducting transition temperature and x-ray diffraction measurements on the three high-pressure phases, InSb-II, InSb-III, and InSb-IV. The locations of the II-III and II-IV phase boundaries have been established. The structure of InSb-IV was found to be hexagonal, and lattice parameters have been determined for all three phases.

The atmospheric pressure phase of RbNiF_3 , which is hexagonal and ferrimagnetic, has been transformed into a high-pressure phase by subjecting it to a pressure of 65 kbars at 600°C . The new phase has the cubic perovskite structure and is antiferromagnetic.

A new antiferromagnetic perovskite, CaCrO_3 , has been prepared by the reaction of CaO and CrO_2 in a gold capsule at a pressure of 65 kbars and temperature of 700°C . The Néel temperature is 90°K at atmospheric pressure and has a pressure coefficient of -0.23°K/kbar . The negative pressure coefficient indicates that the compound exhibits spontaneous band antiferromagnetism.

The martensitic transition and elastic memory exhibited by TiNi have been explained in terms of a structural model which involves the formation of like-atom clusters in the low-temperature phase. Because of cluster formation, deformation of this phase takes place by one-jump slip on adjacent planes, rather than many-jump slip on a single plane. When the sample is heated above the transition temperature, the sample returns to its original shape, since the deformation is removed by one-jump slip in the reverse direction.

IV. PHYSICS OF SOLIDS

Exciton fine structure in the interband magnetoabsorption of germanium has been studied over a wide range of magnetic fields up to 80 kG. The data provide a means of connecting the exciton energy levels in the low field region to those in the high field Landau level region.

Far-infrared cyclotron resonance of free carriers in the conduction band of InSb has been observed at wavelengths of 195, 311 and $337\ \mu$, using a cyanide gas laser as a source and the photoconductivity of the sample as a means of detection. At each wavelength a second absorption peak, associated with transitions between hydrogenic donor impurities, is found on the low field side of the cyclotron resonance peak.

Preliminary measurements have been made of 35- and 70-GHz microwave absorption in $\text{Pb}_{1-x}\text{Sn}_x\text{Te}$ alloys as a function of magnetic field. Two distinct effects have been found: magnetoplasma cyclotron resonance and Shubnikov-de Haas oscillations.

The continuing study of the effect of stress on the spectra arising from donor impurities in silicon has now been extended to bismuth-doped silicon. The effect of stress on the spin-orbit split triplet state has been examined. The value obtained for the pure shear deformation potential coefficient is about 10 percent lower than that previously measured for p-states in either sulfur- or phosphorous-doped silicon.

The theoretical form of the Γ_8 dispersion relations, $\epsilon(\vec{k})$, for the zincblende lattice has been evaluated specifically for HgTe and HgSe by finding the eigenvalues of the $4 \times 4\ \vec{k} \cdot \vec{p}$ interaction

Hamiltonian. Some of the details of the calculated energy surfaces have been compared with experimental Shubnikov-de Haas measurements.

In more basic work, Bloch sums of localized atomic orbitals have been calculated for two one-dimensional models, one in which the orbitals are assumed exponential and the other, Gaussian. Closed form expressions are obtained for various physical quantities and their properties are discussed in some detail. It is found that the effect of orbital overlap is usually greater on the momentum distribution than on the charge density in crystals.

The study of pressure effects on the magnetic properties of MnAs has continued. With MnAs in the high-pressure (B31) phase, the variation of magnetic moment with temperature at pressures ≥ 9 kbars begins to resemble that of MnP, which is isostructural to the B31 MnAs.

In the continuing investigation of magnetic resonance in spiral spin structure compounds, a calculation of the ground state spin configuration of CoCr_2O_4 indicates that a six, rather than a three, sub-lattice model is required to minimize the energy. Using this model, the resonant frequencies are being calculated. Also being investigated, as an aid in understanding resonance behavior in more complicated conical spiral systems, are the ground state properties of a linear chain of two nonequivalent spins; this is the simplest model capable of describing a two sub-lattice conical helix spin configuration.

The Argyres-Kelley decoupling procedure for obtaining the reduced density matrix equations of motion for a system interacting with a bath and an external driving field has been used to find an expression for the contribution of a long wavelength spin wave to the susceptibility of a Heisenberg ferromagnet at low temperatures. The well-known spin wave renormalization and scattering terms are obtained, and in the low temperature limit, the susceptibility due to spin wave has the same form as that obtained using Green's function techniques.

Considering only nearest neighbor spin interactions, an exact solution for the energy, specific heat and susceptibility has been obtained for an open linear chain of arbitrary-dimensional spins and also for a Bethe lattice of coordination number z . A new general Hamiltonian with arbitrary ν -dimensional classical spins and also arbitrary lattice has been set up. This Hamiltonian reduces to the Ising, Vaks-Larkin, Heisenberg and spherical models, respectively, for $\nu = 1, 2, 3$ and ∞ .

Two new features have been observed in the continuing study of stimulated Raman and Brillouin scattering in quartz. A doublet, which can be attributed to coupling of the vibrational mode to the infrared, has been obtained in the Raman spectrum; and iterative backward-forward Brillouin shifts have been achieved directly in the sample without the usual laser reamplification process.

The phonon spectrum of CdTe has been studied at 300° , 77° and 4.2°K by Raman scattering at 1.06μ and far infrared absorption. The Raman studies of the two-phonon spectrum with polarized light and oriented single crystals, exclude the decay of a virtual zone center phonon through the anharmonic phonon interaction as an important Raman process.

Study of the time dependence of thermal defocusing of a laser beam continues. Depending on certain conditions, the change in beam size with time t investigated with a motion picture camera, varies either linearly with t , or as $t^{1/2}$.

CONTENTS

Abstract	iii
Introduction	iv
Organization	x
Reports by Authors Engaged in Solid State Research	xi
 I. SOLID STATE DEVICE RESEARCH	 1
A. Type Conversion and P-N Junctions in n-CdTe Produced by Ion Implantation	1
B. Improved Impedance Properties of $\text{Pb}_{1-x}\text{Sn}_x\text{Te}$ Diodes	3
C. Short Wavelength Response Characteristics of InSb-MOS Photovoltaic Detectors	3
D. Reproducible Electrical Properties of Undoped As-Grown Cadmium Sulfide Platelets	5
E. Etching of Silicon Nitride Using a Thin Deposited Layer of Silicon as an Etch Mask	7
 II. OPTICAL TECHNIQUES AND DEVICES	 11
A. 100-Watt CO_2 Laser Amplifier	11
B. Stable Laser Oscillator, Design and Testing	12
C. Copper-Doped Germanium Detectors	12
D. Magnetically Tuned Semiconductor Lasers for Infrared Heterodyne Measurements	15
E. Excess Noise in Photoconductive Ge:Cu Detectors	17
 III. MATERIALS RESEARCH	 19
A. An Open Tube Reactor for Preparing Compounds with Volatile Constituents	19
B. Crystal Growth from the Vapor Phase by Forced Convection	20
C. Partial Pressures and Thermodynamic Properties in the Si-Te System	23
D. High-Pressure Phase Diagram of InSb	25
E. High-Pressure Perovskite Phase of RbNiF_3	28
F. CaCrO_3 - A New Antiferromagnetic Perovskite	28
G. Like-Atom Cluster Formation and Elastic Memory in TiNi	29

IV. PHYSICS OF SOLIDS	33
A. Electronic Band Structure	33
1. Excitons in Germanium over a Wide Range of Magnetic Fields	33
2. Far-Infrared Cyclotron Resonance in InSb	33
3. Microwave Absorption in $\text{Pb}_{1-x}\text{Sn}_x\text{Te}$	34
4. Optical Studies in Bismuth-Doped Silicon	34
5. Γ_8 Dispersion Relations for HgTe and HgSe	36
6. Some Properties of LCAO Bloch Functions (abstract of paper to be presented at APS Meeting at Berkeley in March 1968)	39
7. Effect of Orbital Overlap on Charge Densities in Crystals (abstract of paper to be presented at APS Meeting at Berkeley in March 1968)	39
8. Effect of Orbital Overlap on Momentum Distributions in Crystals (abstract of paper to be presented at APS Meeting at Berkeley in March 1968)	41
B. Magnetism	
1. Magnetic Properties of High-Pressure-Phase MnAs	41
2. Magnetic Resonance in Spiral Spin Structure Compounds	42
3. Density Matrix Theory and Spin Wave Renormalization	42
4. A Vector Model for Arbitrary-Dimensional Spins: Exact Solution for Linear Chain and Bethe Lattice	44
5. Dependence of Critical Properties on Dimensionality of Spins (abstract of paper scheduled to appear in Phys. Rev. Letters)	46
C. Laser Scattering and Nonlinear Effects	46
1. Stimulated Raman and Brillouin Scattering in Quartz	46
2. Two-Phonon Infrared and Raman Spectrum of CdTe	47
3. Time Dependence in Thermal Defocusing	49

ORGANIZATION

SOLID STATE DIVISION

A. L. McWhorter, *Head*
 P. E. Tannenwald, *Associate Head*
 M. J. Hudson, *Assistant*
 E. P. Warekois

SOLID STATE THEORY

H. J. Zeiger, *Leader*
 M. M. Litvak, *Assistant Leader**

Argyres, P. N.*	Kelley, P. L.
Chinn, S. R.†	Kleiner, W. H.
Dresselhaus, G. F.	Landon, S. N.
Hamilton, D. C.	Larsen, D. M.
Hanus, J.	Palm, B. J.‡
Hartung, W. G.	Sigel, J. L.†
Kaplan, T. A.	Stanley, H. E.

OPTICS AND INFRARED

R. H. Kingston, *Leader*
 R. J. Keyes, *Assistant Leader*

Bates, D. H.	McPhie, J. M.
Bostick, H. A.	Quist, T. M.
Carbone, R. J.	Ross, A. H. M.
Freed, C.	Sullivan, F. M.
Gilmartin, T. J.	Swezey, L.
Hinkley, E. D.	Zimmerman, M. D.
Longaker, P. R.	

ELECTRONIC MATERIALS

J. B. Goodenough, *Leader*
 A. J. Strauss, *Associate Leader*

Anderson, C. H., Jr.	Kasper, H. M.
Andrews, H. I.†	LaFleur, W. J.
Arnott, R. J.	Lavine, M. C.‡
Banus, M. D.	Longo, J. M.
Batson, D. A.	Mastromattei, E. L.
Brebrick, R. F., Jr.	O'Connor, J. R.
Button, M. J.	Owens, E. B.
Capes, R. N.	Plonko, M. C.
DeJaney, E. J.	Raccah, P. M.
England, R. E.	Reed, T. B.
Fahey, R. E.	Roddy, J. T.
Ferretti, A.	Searles, I. H.
Finn, M. C.	Smith, F. T. J.
Iseler, G. W.	Steininger, J. A.
Kafalas, J. A.	Wheatley, G. E.

SOLID STATE PHYSICS

J. G. Mavroides, *Leader*
 G. B. Wright, *Assistant Leader*

Brandt, R. C.	Krag, W. E.
Burke, J. W.	MeIngailis, J.
Carman, R. L.†	Menyuk, N.
Dresselhaus, M. S.*	Murphy, H. C.
Dwight, K., Jr.	NiH, K. W.
Feinleib, J.	Parker, C. D.
Feldman, B.	Perry, F. H.
Fulton, M. J.	Pine, A. S.
Groves, S. H.	Scouler, W. J.
Henrich, V. E.	Stickler, J. J.†
Johnson, E. J.	Strahm, N. D.†
Kernan, W. C.	Tichovolsky, E. J.†
Kolesar, D. F.	Weber, R.

APPLIED PHYSICS

J. O. Dimmock, *Leader*
 T. C. Harman, *Assistant Leader*
 I. MeIngailis, *Assistant Leader*

Brueck, S.†	Donnelly, J. P.	Oliver, M. R.†
Butler, J. F.	Foyt, A. G.	Paladino, A. E.
Calawa, A. R.	Hurwitz, C. E.	Phefan, R. J., Jr.
Carter, F. B.	Lindley, W. T.	Stillman, G. E.
Caswell, F. H.	Matthews, W.†	Ward, J. H. R. III
Clough, T. F.	Mooradian, A.	Wolfe, C. M.
Donaldson, P. L.	Murphy, R. A.†	Youtz, P.

* Leave of Absence

† Research Assistant

‡ Part Time

REPORTS BY AUTHORS ENGAGED IN SOLID STATE RESEARCH

15 November 1967 through 15 February 1968

PUBLISHED REPORTS

Journal Articles*

JA No.			
3021	Localized vs Collective d Electrons and Néel Temper- atures in Perovskite and Perovskite-Related Structures	J. B. Goodenough	Phys. Rev. <u>164</u> , 785 (1967)
3024	Plasmas for High Temperature Chemistry	T. B. Reed	<u>Advances in High Temperature Chemistry</u> , Vol. 1 (Academic Press, New York, 1967)
3038	Long-Term Operation of a Sealed CO ₂ Laser	R. J. Carbone	IEEE J. Quant. Electron. <u>QE-3</u> , 373 (1967)
3044	Optical Properties of the Metal ReO ₃ from 0.1 to 22 eV	J. Feinleib W. J. Scouler A. Ferretti	Phys. Rev. <u>165</u> , 765 (1968)
3049	Characterization and Structure of La ₄ Re ₆ O ₁₉ , a New Metal Cluster Compound	J. M. Longo A. W. Sleight†	Inorg. Chem. <u>7</u> , 108 (1968)
3065	Self-Steepening of Light Pulses	F. De Martini† C. H. Townes† T. K. Gustafson† P. L. Kelley	Phys. Rev. <u>164</u> , 312 (1967)
3066	Magnetic Interactions and Spiral Ground States in Spinels, with Application to ZnCr ₂ Se ₄	K. Dwight N. Menyuk	Phys. Rev. <u>163</u> , 435 (1967)
3068	Theory of the Magnetic Properties of the Ilmenites MTiO ₃	J. B. Goodenough J. J. Stickler	Phys. Rev. <u>164</u> , 768 (1967)
3069	Magnetic Resonance and Suscepti- bility of Several Ilmenite Powders	J. J. Stickler S. Kern† A. Wold† G. S. Heller†	Phys. Rev. <u>164</u> , 765 (1967)

* Reprints available.

† Author not at Lincoln Laboratory.

Reports

JA No.

3074	A 10.6-Micron Four-Port Circulator Using Free Carrier Rotation in InSb	J. H. Dennis	IEEE J. Quant. Electron. <u>QE-3</u> , 416 (1967)
3078	Infrared Heterodyne Detection	M. C. Teich	Proc. IEEE <u>56</u> , 37 (1968)
3086	The Gunn Effect in n-CdTe	M. R. Oliver A. G. Foyt	IEEE Trans. Electron Devices <u>ED-14</u> , 617 (1967)
3090	New Expansion for the Classical Heisenberg Model and Its Similarity to the $S = 1/2$ Ising Model	H. E. Stanley	Phys. Rev. <u>164</u> , 709 (1967)
3097	Perturbation Calculation of Band-Structure Effects in Low-Field Helicon Propagation	A. L. McWhorter J. N. Walpole*	Phys. Rev. <u>163</u> , 618 (1967)
3107	Mode Pulling in a Stimulated Raman Oscillator	P. E. Tannenwald	J. Appl. Phys. <u>38</u> , 4788 (1967)
3110	A New, Widely and Continuously Tunable, High-Power Pulsed Laser Source	R. L. Carman J. Hanus D. L. Weinberg*	Appl. Phys. Letters <u>11</u> , 250 (1967)
3139	Evidence for Electron-TO Phonon Interaction in InSb	D. H. Dickey D. M. Larsen	Phys. Rev. Letters <u>20</u> , 65 (1968)
3148	Imaging and Storage with a Uniform MOS Structure	R. J. Phelan, Jr. J. O. Dimmock	Appl. Phys. Letters <u>11</u> , 359 (1967)
3156	Critical Properties of Isotropically-Interacting Classical Spins Constrained to a Plane	H. E. Stanley	Phys. Rev. Letters <u>20</u> , 150 (1968)
3174	Quartz Raman Laser	P. E. Tannenwald F. H. Perry	Laser Focus <u>3</u> , 17 (1967)
MS-2009	Homogeneity Range and Concentration-Pressure Isotherms of HgSe	R. F. Brebrick A. J. Strauss	<u>Proc. International Conference on II-VI Semiconducting Compounds</u> (W. A. Benjamin, Inc., New York, 1967)

UNPUBLISHED REPORTS

Journal Articles

JA No.

3134A	Epitaxial Gallium Arsenide for High-Efficiency Gunn Oscillators	C. M. Wolfe A. G. Foyt W. T. Lindley	Accepted by Electrochem. Technol.
3149	Magnon-Phonon Coupling in Metallic Films	R. Weber	Accepted by Phys. Rev.

* Author not at Lincoln Laboratory.

JA No.			
3154	Magnetic Ordering and the Electronic Properties of the Heavy Rare Earth Metals	R. E. Watson* A. J. Freeman* J. O. Dimmock	Accepted by Phys. Rev.
3162	Design and Short-Term Stability of Single-Frequency CO ₂ Lasers	C. Freed	Accepted by IEEE J. Quant. Electron.
3169	On Intense Mercury Vapor Green Band Emission	R. J. Carbone M. M. Litvak	Accepted by J. Appl. Phys.
3176	Dependence of Critical Properties on Dimensionality of Spins	H. E. Stanley	Accepted by Phys. Rev. Letters
3185	Self-Trapping in Media with Saturation of the Nonlinear Index	T. K. Gustafson* P. L. Kelley R. Y. Chiao* R. G. Brewer*	Accepted by Appl. Phys. Letters
3187	Isotope Effect in Superconducting Rhenium	E. Maxwell* M. Strongin* T. B. Reed	Accepted by Phys. Rev.
3191	Continuous Operation of a Long Lived CO ₂ Laser Tube	R. J. Carbone	Accepted by IEEE J. Quant. Electron.
MS-1954	Localized vs Collective Descriptions of Magnetic Electrons	J. B. Goodenough	Accepted by J. Appl. Phys.
MS-1955	Magnetic Properties of SrRuO ₃ and CaRuO ₃	J. M. Longo P. M. Racciah J. B. Goodenough	Accepted by J. Appl. Phys.
MS-1956	A Localized-Electron \rightleftharpoons Collective-Electron Transition in the System (La, Sr) CoO ₃	P. M. Racciah J. B. Goodenough	Accepted by J. Appl. Phys.

Meeting Speeches†

MS No.			
1882C	Raman Scattering from Plasmons and Phonons: Experimental	A. Mooradian	Conference on Nonlinear Interactions in Solids, Newport Beach, California, 15 - 19 January 1968
1882D	Raman Scattering from Plasmons and Phonons	G. B. Wright	Colloquium, Polytechnic Institute of Brooklyn, 2 February 1968
1954A	Localized vs Collective Descriptions of Magnetic Electrons	J. B. Goodenough	Interdisciplinary Seminar, Stanford University, 18 - 19 January 1968

* Author not at Lincoln Laboratory.

† Titles of Meeting Speeches are listed for information only. No copies are available for distribution.

Reports

MS No.

1980A	Modern High Pressure Techniques	J. A. Kafalas	} ASM, High Pressure Treatment of Materials, ManLabs, Inc., Cambridge, Massachusetts, 16 - 17 November 1967
2015A	Survey of Equipment for High Pressure Studies	M. D. Banus	
2016A	Retained High Pressure Phases and High Pressure Synthesis	M. D. Banus	
1996B	Electron-Beam-Pumped Semiconductor Lasers	C. E. Hurwitz	Colloquium, Cornell University, 7 February 1968
2111	Magnetorefectivity of Bismuth	M. S. Maltz M. S. Dresselhaus	} American Physical Society, New York, 16 - 18 November 1967
2141	Zero Gap Semiconductors	S. H. Groves	
2146	Band Structure, Preparation, and Device Potentialities of $\text{Hg}_x\text{Cd}_{1-x}\text{Te}$ and $\text{Pb}_{1-x}\text{Sn}_x\text{Te}$	T. C. Harman	
2131	On Emission and Absorption by Excited OH Λ -Doublet States	B. Zuckerman* D. F. Dickinson* M. M. Litvak	American Astronomical Society, University of Pennsylvania, 4 - 7 December 1967
2138	Raman Scattering from Elementary Excitations in Solids Using Lasers	A. Mooradian	Seminar, M. I. T., 17 November 1967
2141A	Zero Gap Semiconductors	S. H. Groves	Seminar, Tufts University, 19 January 1968
2149A	Infrared Detection and Imaging Using an InSb MOS Structure	J. O. Dimmock	Seminar, Harvard University, 6 December 1967
2151	Critical Properties of the Vaks-Larkin Model for the λ Transition in a Bose Fluid	H. E. Stanley	Statistical Mechanics Meeting, Yeshiva University, 15 November 1967
2153	CO ₂ Laser Systems: Generation, Transmission and Detection of Coherent Infrared Waves	R. H. Kingston	Colloquium, Columbia University, 12 January 1968
2162	Band Structure, Materials Preparation and Device Possibilities in the Pb-Sn Salt Systems	T. C. Harman	Seminar, P. R. Mallory & Co., Inc., Burlington, Massachusetts, 6 December 1967
2164	Infrared Imaging and Memory with an InSb MOS Structure	R. J. Phelan, Jr.	Seminar, M. I. T., 1 December 1967

* Author not at Lincoln Laboratory.

MS No.

2209	Growth, Annealing, and Properties of Lead-Tin Chalcogenides	T. C. Harman	Industrial Liaison Symposium on Electronic Materials and Devices, M.I.T., 13 February 1968
2229	Lead-Tin Chalcogenide Infrared Detectors and Lasers	I. Melngailis	
2258	Infrared Detection, Imaging and Storage Using an InSb MOS Structure	R. J. Phelan, Jr.	
2259	Growth of Epitaxial GaAs for X-Band Gunn Effect Oscillators	C. M. Wolfe	
2215	Electronic Raman Scattering from Impurities in Semiconductors	G. B. Wright	Conference on Nonlinear Interactions in Solids, Newport Beach, California, 15 - 19 January 1968
2239	Raman Scattering from Plasmons and Phonons: Theoretical	A. L. McWhorter	
2223	Electronic Structure of Nickel: Theory and Experiments	J. Hanus	American Physical Society, Chicago, 29 January - 1 February 1968
2224	Interpolation Scheme for Energy Bands in Cu and Ni	G. F. Dresselhaus J. Hanus	International Symposium on Atomic, Molecular, and Solid State Theory and Quantum Biology, Sanibel Island, Florida, 15 - 20 January 1968
2228	Interpolation Methods for Phonon Spectra in Crystals	G. F. Dresselhaus M. S. Dresselhaus	
2230	Spin Resonance in Magnetic Spiral Structures	H. J. Zeiger	Seminar, Boston College, 17 January 1968
2249	Ultraviolet and Infrared Pumping of OH Molecules	M. M. Litvak	HII Region Symposium, Charlottesville, Virginia, 8 - 11 December 1967

I. SOLID STATE DEVICE RESEARCH

A. TYPE CONVERSION AND P-N JUNCTIONS IN n-CdTe PRODUCED BY ION IMPLANTATION

We have produced type conversion and made p-n junctions in n-type CdTe by the implantation of 400 keV arsenic ions. In this section, the details of the implantation procedure and sample processing are discussed. Some preliminary device results on p-n junctions are also given. We believe that this is the first report of successful type conversion produced by ion implantation in a II-VI compound semiconductor.

Although chemical doping by ion implantation has been studied extensively in silicon and germanium (see, for example, Refs. 1 and 2), and to a lesser extent in GaAs^{3,4} and SiC^{5,6}, very little success has been achieved by ion implantation in II-VI semiconducting compounds. Indium⁷ and cadmium⁸ ions have been implanted into thin films of CdTe. The results of these experiments did not, however, show evidence of chemical doping due to the implanted ion. Several additional problems are encountered in attempting to chemically dope these materials by ion implantation. Their high vapor pressure hinders hot implantation, which, as discussed below, appears to be necessary for successful type conversion. Sample preparation and post annealing are also complicated by stoichiometric changes and self-compensation effects⁹⁻¹¹ which occur at fairly low temperatures.

The ion accelerator used in these experiments is a modified 400-kV Van de Graaff generator. Arsenic ions are produced by the RF excitation of arsine gas, accelerated to 400 keV and magnetically analyzed. The accelerator drift tube is evacuated using a turbo-molecular pump with an auxiliary VacIon pump mounted at the sample chamber. During implantation, the entire system is held at approximately 10^{-6} torr. The sample holder is a tantalum block which may be heated between room temperature and 550°C.

The CdTe samples (approximately $10 \times 5 \times 1$ mm) were cut from as-grown ingots of Bridgman-grown CdTe and pre-annealed in cadmium vapor for two days at 650°C to insure n-type conductivity.

The results of initial room temperature implantations indicated that the introduced radiation damage, which caused the implanted layer to be semi-insulating, does not anneal out within two days at temperatures up to 650°C. Hot implantation, used successfully in silicon to anneal out radiation damage as it occurs, was indicated. Due to the high vapor pressure of CdTe, however, it is impossible to heat the samples in vacuum over 250°C. It was found that a 1500-Å SiO₂ layer deposited by a silane-oxygen reaction, could be used to prevent evaporation and thermal etching while allowing a majority of the arsenic ions to reach the sample. (This combination is currently limited to sample implantation temperatures under about 525°C due to the crazing of the oxide above this temperature.) The oxide layer has the further advantage of reducing surface sputtering of the sample during implantation. Using SiO₂ encapsulated samples, it was found that implantation temperatures greater than 475°C were needed to achieve measurable sheet conductivity without post-annealing. Implantations were therefore done at sample temperatures of 500°C. The samples were bombarded with a 400-keV arsenic ion current of $0.5 \mu\text{A}/\text{cm}^2$ for 15 minutes, giving a total dose of $\sim 3 \times 10^{15}/\text{cm}^2$.

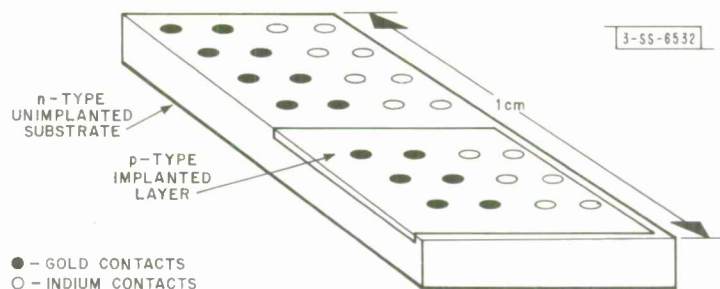


Fig. I-1. Sketch of typical implanted CdTe sample after gold and indium contacts have been plated onto it.

After implantation, the samples were cooled to room temperature and the SiO_2 removed. The presence of arsenic was confirmed in several samples by electron probe analysis. Each sample was then post-annealed at 650°C in an ampoule with cadmium and CdTe powder. This post-anneal was necessary to insure that the substrate remained n-type and that any type conversion in the implanted layer was not caused by stoichiometric changes due to heating effects. Following a water quench to room temperature, each sample was removed from its ampoule, and the top surface plated with small gold and indium contacts using photoresist as a plating mask. The resulting sample configuration is illustrated in Fig. I-1 where the dimensions of the implanted region are approximately $4\text{ mm} \times 4\text{ mm} \times 0.3\text{ }\mu\text{m}$. (Previous experiments had shown that plated indium contacts are ohmic to n-CdTe, and that gold contacts are ohmic to p-CdTe.)

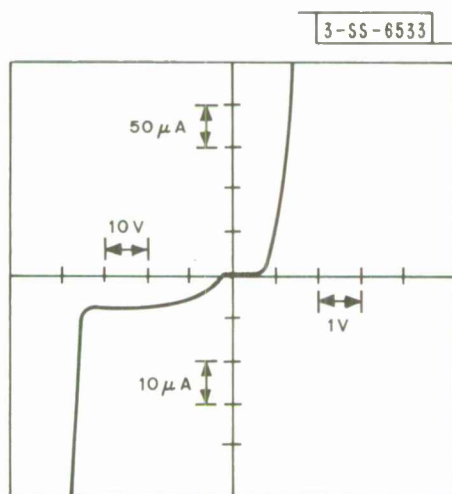


Fig. I-2. Room temperature current-voltage characteristic for a diode between a gold contact on the p-type implanted layer and a nearby indium contact on the unimplanted n-type substrate.

As an initial electrical test, a DC thermal probe was used between adjacent contacts to indicate conductivity type. This test showed that in these samples the implanted layer had, in fact, been converted to p-type while the substrate remained n-type. As a second test, Hall effect measurements were made using four adjacent contacts on the implanted layer and again on the unimplanted substrate. As above, the implanted layer was found to be p-type and the substrate n-type. The hole concentration in the implanted region, however, was about a factor of 10^{-2} to 10^{-3} below the calculated concentration of implanted ions. Although this may be due to self-compensation, the low Hall mobility ($\mu_p \sim 3\text{ cm}^2/\text{V sec}$) suggests that unannealed radiation damage may still be present. As a final check, the current-voltage characteristics between the various contacts were examined. We found that the gold contacts on the implanted layer were ohmic, with a contact-contact resistance of about 50 to 100 kilohms, and that the indium contacts on the unimplanted layer were also ohmic with a resistance of about 25 ohms. Diode characteristics were observed between gold contacts on the implanted layer and indium contacts on the unimplanted substrate. These diodes had forward resistances of about 30 ohms, and sharp reverse breakdowns of about 40 volts. A current-voltage characteristic of one of the best diodes is shown in Fig. I-2. Note the scale changes between the forward and reverse characteristics.

Finally, for diodes biased at currents greater than 2 ma in the forward direction, infrared radiation was observed from beneath the gold contact on the implanted region. By using a set of interference filters, the wavelength of this radiation was determined to be approximately 0.88μ corresponding to that of band gap radiation in CdTe at room temperature.

In order to establish that the p-type conversion of the implanted layer was caused by chemical doping and not radiation damage, implantations were repeated as above except that argon, instead of arsenic, was used as the implanted ion. The implanted layers of these samples remained n-type indicating that the p-type conversion following the arsenic implantation was due to chemical doping of the n-CdTe by the arsenic.

J. P. Donnelly W. T. Lindley
A. G. Foyt J. O. Dimmock
E. D. Hinkley

B. IMPROVED IMPEDANCE PROPERTIES OF $\text{Pb}_{1-x}\text{Sn}_x\text{Te}$ DIODES

The volt-ampere characteristics of a number of $\text{Pb}_{1-x}\text{Sn}_x\text{Te}$ diodes have been greatly improved by an electrolytic etching procedure.¹² The diodes were fabricated from vapor-grown annealed $\text{Pb}_{1-x}\text{Sn}_x\text{Te}$ by methods previously described.¹³ The diodes were then etched for 3 minutes at a rate of approximately 10μ per minute and thoroughly rinsed in distilled water. Figure I-3 shows the volt-ampere characteristics of an etched $\text{Pb}_{0.85}\text{Sn}_{0.15}\text{Te}$ diode at 77°K which exhibits an impedance near zero-bias of approximately 2000 ohms. At 12°K the zero-bias impedance was 5000 ohms. Before etching, the impedance of this diode was about 3 ohms at both temperatures. The etching process caused the zero-bias impedance of a $\text{Pb}_{0.8}\text{Sn}_{0.2}\text{Te}$ diode to increase from 5 to 20,000 ohms at 12°K and from 3 to 10 ohms at 77°K .

Previously, $\text{Pb}_{1-x}\text{Sn}_x\text{Te}$ diodes with $x > 0.09$ have had zero bias impedances of 100 ohms or less and generally near 5 ohms. The present results indicate that the surface condition of $\text{Pb}_{1-x}\text{Sn}_x\text{Te}$ diodes plays an important part in determining the zero-bias impedance and that this impedance can in some devices be increased by suitable surface preparation. This offers the possibility of greatly improving the performance of $\text{Pb}_{1-x}\text{Sn}_x\text{Te}$ photovoltaic detectors. It has been shown that the detectivity of a photovoltaic detector limited by thermal noise is proportional to the square-root of the zero bias impedance.¹⁴ In addition, preliminary experimental results indicate that the threshold current of diode lasers is substantially reduced by the etching process.

J. F. Butler

C. SHORT WAVELENGTH RESPONSE CHARACTERISTICS OF InSb-MOS PHOTOVOLTAIC DETECTORS

In this section we report the initial results of a study of the spectral response of InSb-MOS detectors¹⁵ over the region from about 5 to 0.25μ . Using a prism spectrometer with an SiO_2

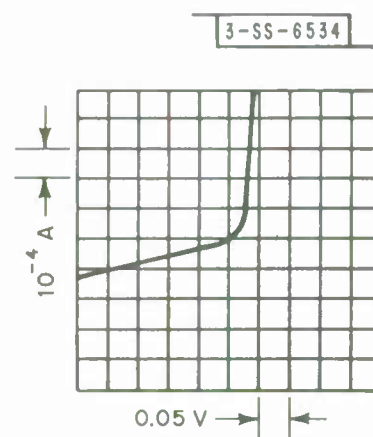


Fig. I-3. Current voltage characteristics of an etched $\text{Pb}_{0.85}\text{Sn}_{0.15}\text{Te}$ diode at 77°K .

* The $\text{Pb}_{1-x}\text{Sn}_x\text{Te}$ crystals were grown, annealed and junctions diffused by T. C. Harman.

Section I

prism and a xenon arc as a source we find that between 77° and 300°K there is a photovoltage developed across the MOS structure at photon energies between about 1 and 5 eV. When this photovoltage is compared with that developed by a Reeder diamond window thermocouple, we find that the MOS photovoltage has a single broad peak at about 4 eV. The results of these measurements are shown in Fig. I-4. The measurements were made at 300°, 195° and 77°K, with the

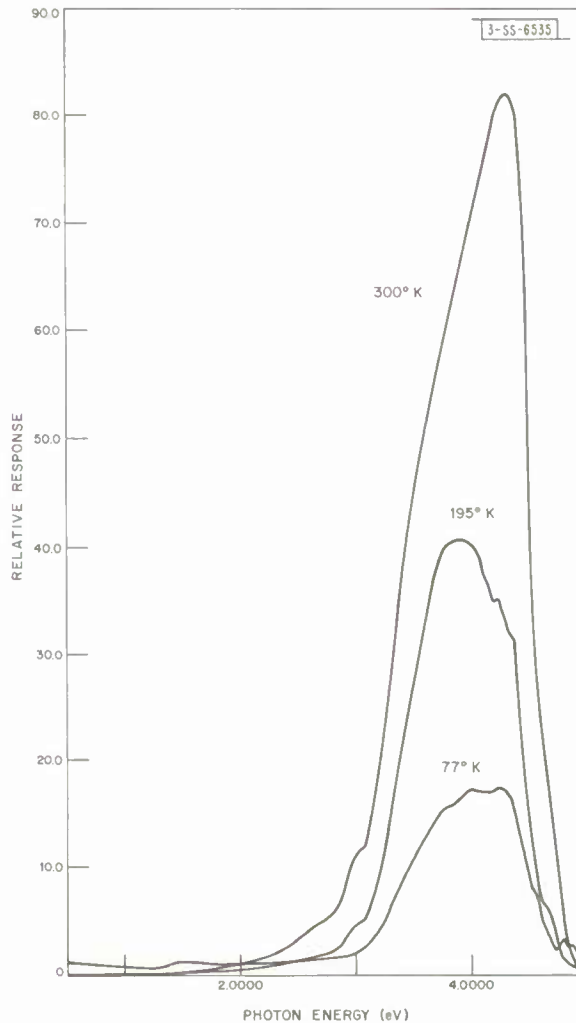


Fig. I-4. Relative photovoltaic response of an InSb-MOS detector to radiation between 0.5 and 5 eV at 77°, 195° and 300°K.

room darkened and with the photon energy increasing with time. The monochromatic beam was chopped at 13 Hz, and the output photovoltaic signal was amplified by a PAR Model HR-8. The amplifier output was fed to the Vidar data acquisition system and over a telephone line to an IBM Model 40 computer where the data was recorded on magnetic tape. Subsequent reduction of the data, including the data plotting, is then performed entirely by the Lincoln Laboratory computer facility.

Measurements of the response of the MOS detector to near IR radiation while the detector is being irradiated with light of a different energy are under way in the expectation that this will

clarify the operational mechanisms of the detector. We find, for example, that there are long-lived states of the detector which can be changed by irradiating the detector with UV or visible light. We expect to find that this effect is related to the MOS detector response discussed previously¹⁵ and to the photovoltage observed around 4 eV shown in Fig. I-4.

W. E. Krag
R. J. Phelan, Jr.
J. O. Dimmock

D. REPRODUCIBLE ELECTRICAL PROPERTIES OF UNDOPED AS-GROWN CADMIUM SULFIDE PLATELETS

A number of CdS platelets grown under similar conditions have been investigated to determine the feasibility of obtaining crystals with reproducible electrical properties without doping or additional processing.

These crystals were grown by a modification of Frerichs'¹⁶ method using elemental cadmium and sulfur as source materials in a flowing hydrogen atmosphere. A diagram of the growth apparatus is shown in Fig. I-5. To separately control the temperature of the sulfur, the cadmium,

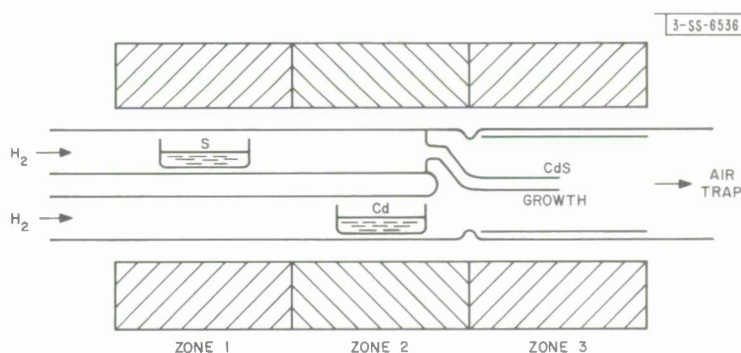


Fig. I-5. Growth apparatus for CdS platelets.

and the growth region, a three-zone furnace was used. The furnace tube and boats are made of spectrosil quartz and a liner tube is used in the growth region to facilitate removal of the crystals. The input tubes are 25 mm in diameter and the growth region is 35 mm in diameter. Control temperatures in this investigation were 300°C for the sulfur, 600°C for the cadmium, and 950°C for the growth region. Hydrogen from a palladium-alloy diffuser was passed over the sulfur (producing H_2S) and over the cadmium at rates of 200 ml/min. Under these conditions a large number of platelets were grown in a period of 2 to 3 hours.

Platelets from which 4- to 6-mm squares could be cleaved were selected as measurement samples. Ohmic contacts were made by alloying 10-mil diameter indium spheres on the corners of the samples at 200°C in a hydrogen atmosphere. This contacting procedure has been found to have no apparent effect on the as-grown electrical properties.

The van der Pauw¹⁷ method was used to measure resistivity ρ and Hall constant R_H . Measurements were taken at 300° and 77°K only. The resulting data are estimated to be accurate to about ± 10 percent with the largest part of the error being introduced in the thickness measurement. Carrier concentration was calculated from $n = 1/eR_H$, where e is the electronic charge,

TABLE I-1
INTRA-RUN ELECTRICAL PROPERTIES

300°K			77°K		
ρ (ohm-cm)	n (cm ⁻³)	μ (cm ² /V sec)	ρ (ohm-cm)	n (cm ⁻³)	μ (cm ² /V sec)
2.5	8.1×10^{15}	310	1.7	9.3×10^{14}	3900
3.2	6.6×10^{15}	300	2.5	6.0×10^{14}	4200
2.4	1.1×10^{16}	280	0.75	1.9×10^{15}	4400
1.8	1.0×10^{16}	340	1.7	1.1×10^{15}	4100
2.0	8.8×10^{15}	350	1.5	8.4×10^{14}	5000
Average Value and Average Deviation					
2.4	8.9×10^{15}	316	1.6	1.1×10^{15}	4300
±16%	±14%	±7%	±25%	±32%	±7%

and the Hall mobility from $\mu_H = R_H/\rho$. The mobility values are independent of thickness errors, such that the error in determining mobility should be smaller than the error in determining resistivity and carrier concentration.

Data for five platelets from the same run are collected in Table I-1. At the bottom of each column is the average value of the property in the column and the average deviation from that value expressed as a percentage. In view of the thickness measurement error of ±10 percent, the variation in the 300°K resistivity (±16 percent) and the carrier concentration (±14 percent) is quite reasonable. The average deviations in 77°K resistivity (±25 percent) and carrier concentration (±32 percent) are somewhat larger and may reflect differences in impurity content from platelet to platelet. The low average deviations in 300° and 77°K mobilities (±7 percent) are due to the thickness error independence mentioned above and the fact that mobility is not strongly dependent on concentration in this resistivity range. The last crystal in Table I-1 has mobility values which are comparable to the best reported for CdS. These numbers probably represent the upper mobility limit due to piezoelectric and optical mode scattering.¹⁸

Results of a series of nine runs performed under similar conditions are shown in Table I-2. Each run has been characterized by an average of the properties of two or more platelets. Here the average values for the runs and the average deviations have been listed at the bottom of each column. As before, somewhat larger deviations in the resistivity and carrier concentration are observed at 77°K than at 300°K. These average variations reflect measurement error and differences in the properties of the platelets within a run (as in Table I-1) as well as run-to-run variations.

TABLE I-2
INTER-RUN ELECTRICAL PROPERTIES

300°K			77°K		
ρ (ohm-cm)	n (cm ⁻³)	μ (cm ² /V sec)	ρ (ohm-cm)	n (cm ⁻³)	μ (cm ² /V sec)
2.2	9.1×10^{15}	320	3.4	7.5×10^{14}	3400
1.0	1.9×10^{16}	310	0.61	2.1×10^{15}	5000
2.0	1.2×10^{16}	280	1.5	1.0×10^{15}	4100
0.67	3.1×10^{16}	300	0.59	2.4×10^{15}	4300
1.5	1.4×10^{16}	300	1.5	1.1×10^{15}	3800
1.1	1.9×10^{16}	320	0.49	3.9×10^{15}	3300
1.4	1.3×10^{16}	340	0.56	2.8×10^{15}	3900
1.8	1.1×10^{16}	330	0.79	2.0×10^{15}	4000
3.1	5.7×10^{15}	360	2.3	6.6×10^{14}	4100
Average Value and Average Deviation					
1.6 ±34%	1.5×10^{16} ±37%	320 ±6%	1.3 ±60%	1.9×10^{15} ±47%	4000 ±9%

We conclude that undoped as-grown CdS platelets with given electrical properties can be obtained with a good degree of success. By suitable variations in growth conditions one should be able to control the conductivity of undoped as-grown CdS platelets over some range of values as yet to be determined.

C. M. Wolfe
L. Krohn, Jr.

E. ETCHING OF SILICON NITRIDE USING A THIN DEPOSITED LAYER OF SILICON AS AN ETCH MASK

A technique has been developed for etching patterns in silicon nitride layers using a thin layer of silicon as an etch mask. This layer is deposited over the silicon nitride using the same reactor system as was used in depositing the silicon nitride and hence no additional equipment or transferring of wafers is required. Patterns are etched in the silicon over-layer using standard photolithographic techniques. Concentrated hydrofluoric or hot phosphoric acid can then be used to remove the exposed areas of silicon nitride.

This technique solves one of the primary problems which arises in attempting to use a silicon nitride layer as a diffusion mask or as a junction encapsulation material. Because of the long etching times and strong etchants required to remove silicon nitride, the photo resists and

Section I

techniques which have been used with silicon dioxide do not work well with silicon nitride. Methods for etching silicon nitride have been reported^{19,20} using layers of other materials deposited over the silicon nitride for an etch mask. These methods have involved additional equipment and handling of wafers.

The silicon nitride is deposited from the reaction of silane and ammonia diluted with nitrogen at a temperature of 600°C. No claim is made that this material is precisely Si_3N_4 . It has been used as a diffusion mask in making GaAs diodes and as an insulator in a MIS structure on GaAs. It has an etch rate in concentrated hydrofluoric acid of 200 Å per minute and an etch rate in 180°C reflux boiling phosphoric acid of 300 Å per minute. The silicon layer is deposited by decomposing silane at 600°C. The same system is also used for the deposition of silicon dioxide at 300°C using the reaction of silane and oxygen.

The reaction chamber used is cylindrical, 4½ inches in diameter and 4 inches high, with the lower half stainless steel and the top half glass. The samples are heated on a 1-inch wide graphite heater strip located near the center of the chamber. The reacting gases are introduced through a 1-inch diameter gas dispersion frit located over the samples. Table I-3 shows the gas flow rates through the frit and the deposition rates. Additional nitrogen is also introduced into the reaction chamber through separate tubes at a rate of 4 liters/min.

TABLE I-3 DEPOSITION CONDITIONS AND RATES FOR SILICON AND SILICON NITRIDE			
Deposited Material	Deposition Temperature	Gas Composition	Deposition Rate
Silicon Nitride	600°C	1 liter/min N_2 0.002 liter/min SiH_4 0.08 liter/min NH_3	1200 Å/min
Silicon	600°C	1 liter/min N_2 0.002 liter/min SiH_4	700 Å/min

In a normal run the silicon nitride layer of the desired thickness is first deposited, followed by the 500-Å thick silicon etch mask. The silicon nitride reaction can be stopped either by lowering the temperature below 400°C or by turning off first the silane and then the ammonia gas. The gradual transition from silicon nitride to silicon that results if the ammonia is turned off while the sample is at 600°C does not give good results. Nitrogen is used for purging the system both before the deposition run and between steps of the run.

The next step after the sample is removed from the deposition chamber is to apply the photo resist and process it to obtain the desired pattern. Openings are then etched in the silicon layer using an etchant composed of hydrofluoric, nitric, and acetic acids in the ratio 1:3:8. Next the silicon nitride is removed in the desired areas using concentrated hydrofluoric acid or reflux

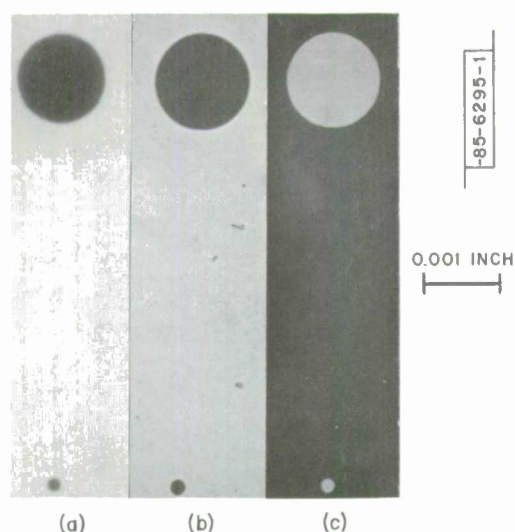


Fig. I-6. Photomicrographs of (a) photographic mask, (b) pattern in silicon etch mask, and (c) final pattern in silicon nitride.

in the silicon nitride. These results are typical of those normally obtained. However, even better resolution has been obtained with more careful control of the timing of the etching steps. In general, the results obtained using the silicon etch mask over silicon nitride have been as good as those obtained using the same photolithographic techniques on silicon dioxide.

boiling phosphoric acid at 180°C. The final step is the removal of any remaining photo resist and the silicon layer. Since the silicon etch mask is so thin, even if the etchant used to remove it attacks the sample, only very slight etching of open areas of the sample will occur.

These same steps can be used to etch openings in layered structures of silicon nitride over silicon dioxide. In this case hot phosphoric acid should be used as the etchant for the silicon nitride since, as reported by van Gelder and Hauser,¹⁹ it does not rapidly attack silicon dioxide. After the silicon nitride has been etched and the silicon etch mask removed, the silicon dioxide remaining in the openings can be removed with buffered hydrofluoric acid.

Figure I-6 presents a comparison of three photomicrographs showing the photographic mask, the pattern in the silicon etch mask, and the final pattern

W. T. Lindley

REFERENCES

1. J.O. McCaldin, Progress in Solid State Chemistry (Macmillan, New York, 1965), Vol. 2, Ch. 2.
2. Nucl. Instruments Methods 38, 1 - 322 (1965).
3. J.W. Mayer, O.J. Marsh, R. Mankarious, and R. Bower, J. Appl. Phys. 38, 1975 (1967).
4. J.B. Schroeder and H.D. Dieselman, Proc. IEEE 55, 125 (1967).
5. F.A. Leith, W.J. King, and P. McNally, "High Energy Ion Implantation of Materials," Final Report, Contract AF 19(628)-4970, Ion Physics (1967).
6. H. Dunlap, O.J. Marsh, J.W. Mayer, and G.A. Shifrin, "Development of Ion Implantation Techniques for Micro-electronics," QPR 4, Contract NAS12-124, Hughes Research Laboratory, 1967 (unpublished).
7. G.A. Kachurin, A.E. Gorodetskii, Yu. V. Loburets, and L.S. Smirnov, Soviet Physics - Solid State 9, 375 (1967).
8. L.S. Smirnov, G.A. Kachurin, and A.E. Gorodetskii, Soviet Physics - Solid State 9, 564 (1967).
9. G. Mandel, Phys. Rev. 134, A1073 (1964).
10. R.S. Title, G. Mandel, and F.F. Morehead, Phys. Rev. 136, A300 (1964).
11. G. Mandel, F.F. Morehead, and P.R. Wagner, Phys. Rev. 136, A826 (1964).
12. M.K. Norr, "Polishes and Etches for Tin Telluride, Lead Sulfide, Lead Selenide and Lead Telluride," Report No. NOLTR63-156, U.S. Naval Ordnance Laboratory, White Oak, Maryland (1963).
13. J.F. Butler, A.R. Calawa, and T.C. Harman, Appl. Phys. Letters 9, 427 (1966).
14. Solid State Research Report, Lincoln Laboratory, M.I.T. (1967:4), p.1.
15. R.J. Phelan, Jr. and J.O. Dimmock, Appl. Phys. Letters 10, 55 (1967); 11, 359 (1967).
16. R. Frerichs, Phys. Rev. 72, 594 (1947).
17. L.J. van der Pauw, Philips Res. Rep. 13, 1 (1958).
18. S.S. Devlin, Physics and Chemistry of II-VI Compounds, M. Aven and J.S. Prener, Eds. (Interscience Publishers, New York, 1967), p.551.
19. W. van Gelder and V.E. Hauser, J. Electrochem. Soc. 114, 869 (1967).
20. P.M. Brown, W.E. Engeler, M. Garfinkel, and F.K. Herman, J. Electrochem. Soc. 114, 730 (1967).

II. OPTICAL TECHNIQUES AND DEVICES

A. 100-WATT CO₂ LASER AMPLIFIER

The 9-meter CO₂ amplifier mentioned in the previous Solid State Research Report¹ has been completed and initial measurements of insertion loss, gain and beam distortion have been taken. The data were taken with a flowing gas mixture of 1.3 torrs CO₂, 1.4 torrs N₂, and 4.8 torrs He with the fine flow adjustment for each of the three equal length tubes made with a throttle valve. The tubes of 20, 25, and 30 mm bore, listed in order of beam traversal, used sodium chloride windows set at 5° off normal. With the discharge off, the attenuation was 15, 23, and 19 percent for the tubes in the order listed above. The water-cooled amplifier tubes are shown in Fig. II-1 with the smallest bore tube at the left and the largest bore tube on the right. The input at the rear of the 20-mm bore tube (background left) is from a beam expander-collimator which accepts an input beam from a Brewster window CO₂ laser.

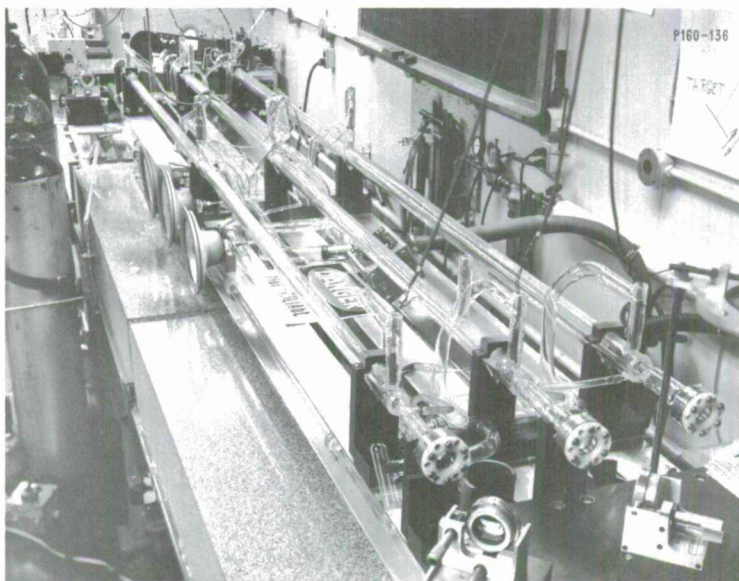


Fig. II-1. 100-watt amplifier for CO₂ 10.6- μ m radiation.

When the amplifier tubes are discharged, the total gain for the three tubes with a 5-W input is 13.1 db which may be broken down to 6.5-, 3.8-, and 2.8-db gains in the 20-, 25-, and 30-mm bore tubes, respectively. The output 10.6- μ m beam at 102 W indicates an efficiency of about 11.5 percent relative to the electrical power input. Saturation is becoming important especially in the largest bore (greatest power input) tube but the gain is still considerably greater than 1.0.

The input beam in the TEM₀₀ mode is 1-cm diameter and the output from the amplifier is 1.6-cm diameter with no great visible amount of shape distortion. This was checked with several different input modes which were also reproduced at the high power output of the amplifier.

R. J. Carbone

Section II

B. STABLE LASER OSCILLATOR, DESIGN AND TESTING

The short-term stability measurements on a single-frequency CO_2 laser described in the previous Solid State Research Report¹ were submitted and accepted for publication by the IEEE Journal of Quantum Electronics.

A $1\frac{1}{2}$ -meter cavity stable laser is currently being tested. This tube is a scaled-up version of the 50-cm cavity lasers described previously and in the preliminary measurements has yielded single-frequency output powers up to 15 W without optimizing either the output coupling or the gas fill. Within more than two orders of magnitude in power, single transition output was obtained without any use of a dispersive prism or grating. It was interesting to see that such single transition output was easily obtained even on the $1\frac{1}{2}$ -meter cavity laser which is not as yet equipped with a mirror tuner. However, in spite of the 100-MHz cavity mode spacing, this laser would only oscillate in the $00^{\circ}1$ to $02^{\circ}0$ vibrational band of CO_2 during several weeks of continuous testing. Although systematic variations of pressure and excitation current have been tried over more than a 2:1 range, the output would at most shift to some other strong P- or R-branch rotational transition within the $00^{\circ}1$ to $02^{\circ}0$ vibrational band.

By using a scratched output mirror the laser was finally forced to oscillate in off-axis radial modes in the $00^{\circ}1$ to $10^{\circ}0$ vibrational band. Under this operating condition the beat note of the $1\frac{1}{2}$ -meter cavity and a tunable 50-cm cavity stable laser was obtained. Spectrum analyzer displays of the beat note indicated a short-term frequency stability of the same order of magnitude as was previously observed with two 50-cm cavity tubes.

Extensive spectrometer measurements were also carried out with the tunable 50-cm laser. This tube would only oscillate in $00^{\circ}1$ to $10^{\circ}0$ vibrational band transitions with axial tuning of approximately 80μ . Single transition outputs up to at least three orders of magnitude in power were obtainable with the tunable laser.

Extensive modifications of the stable laser design have been carried out and completed. The assembly and testing of the new tubes is about to begin.

C. Freed

C. COPPER-DOPED GERMANIUM DETECTORS

Cu-Ge detectors have been fabricated for low level detection in the 8- to $12\text{-}\mu$ region. A cooled FET circuit was used to measure noise equivalent powers as low as 10^{-15} W. Near theoretical operation has been obtained for these low background powers.

Copper-doped germanium detectors were fabricated from single crystal germanium with a net donor impurity concentration of $N_d \sim 7.4 \times 10^{11}$ atoms per cm^3 and liquid nitrogen temperature mobility $\mu \sim 4.75 \times 10^4 \text{ cm}^2$ per volt sec. Copper was evaporated on the etched surfaces of germanium wafers and the diffusions were made in a gas flow of 85 percent argon, 15 percent hydrogen for about 18 hours at a temperature of 745°C . The wafers were removed from the hot furnace and placed on an aluminum block to speed the cool-down process. The resulting copper concentration in these samples is approximately 7×10^{15} atoms per cm^3 . The wafers were then sawed into 3-mm cubes, etched, and two indium contacts soldered to opposite faces of the cube. After being cleaned, the devices were given an additional slight etch. One contact was soldered to a copper block and a small lead attached to the other contact.

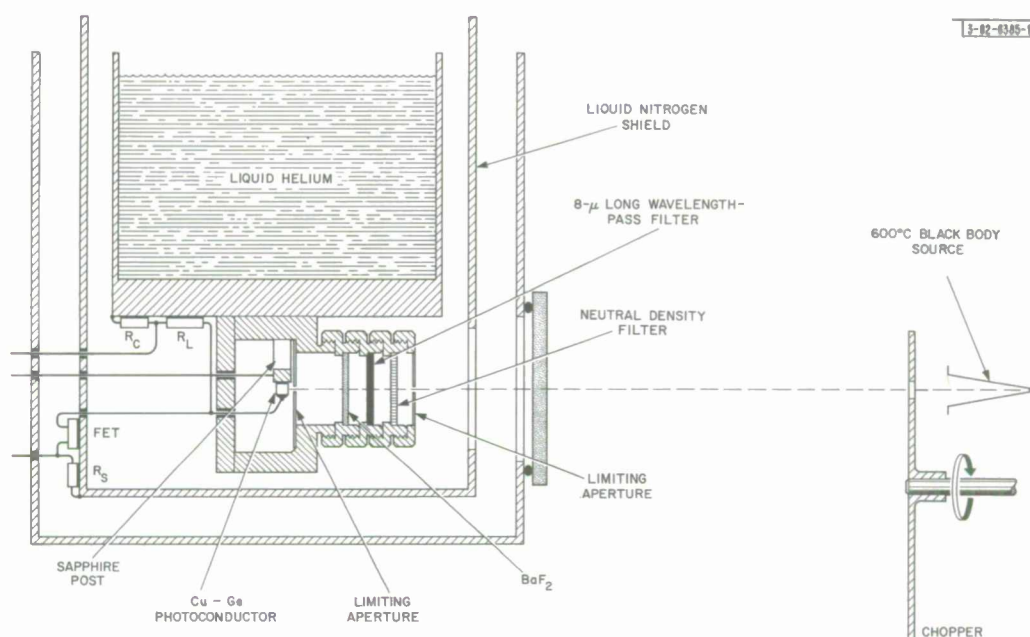


Fig. II-2. Artist's sketch showing physical relationship between detector, filters, cooled FET circuit, and black body source.

Figure II-2 shows the experimental arrangement used. The detector was electrically isolated from the dewar by mounting it on a sapphire post. Radiation falling on the detector was limited to the 8- to 12- μ wavelength region by placing an 8- μ long wavelength-pass filter and barium fluoride at the cold temperature. In order to control the power falling on the detectors, limiting apertures and neutral density filters were placed in front of the detector and at the cold temperature. The signal source for obtaining the responsivity R was a 600°C black body source chopped at various frequencies less than 1000 Hz. Figure II-2 also shows the physical location of part of the measurement circuitry. The FET and source resistor R_S were located on the liquid nitrogen shield and the load resistor R_L and current measuring resistor R_C mounted on the liquid helium block.

The complete electrical circuit is shown in Fig. II-3. A low noise field effect transistor, operated as a source follower, was used to transform the high load impedance (in some cases 40 megohms) to a more workable value in the kilohm range (voltage gain of 0.9). The metal film load resistor R_L was also located at the cold temperature to reduce its thermal noise power, and the FET was located on the liquid nitrogen shield to insure a negligible gate current. The DC current through the detector could be measured directly as a voltage across R_C . This circuit arrangement allows the measurement of very low noise voltages. For our measurements the minimum noise was the thermal noise of the load resistor R_L , located at liquid helium temperature.

In Fig. II-4 is shown a typical responsivity-electric field (R vs E) curve for incident radiation between 8 and 12 μ . We have found this curve to be the same for all values of background and signal intensities measured. The shape of the I - V curve is symmetrical about the origin, i.e., for either polarity of applied voltage.

Section II

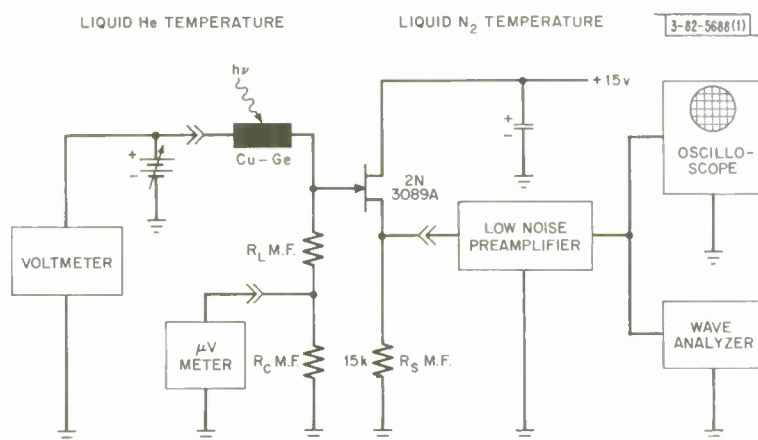


Fig. II-3. Circuit used to measure the responsivity and NEP.

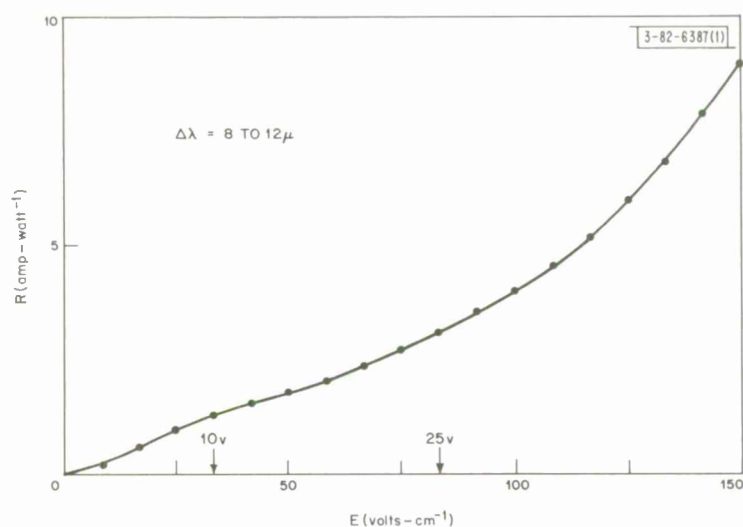


Fig. II-4. Plot of response in amperes per watt vs the electric field in volts per cm.

The noise equivalent power (NEP) was measured as a function of background power between 3×10^{-5} W and about 10^{-11} W in the 8- to 12- μ region. The noise voltage was measured at frequencies of 500 Hz and below and at a bandwidth of 10 Hz. The noise equivalent power as a function of background power is shown in Fig. II-5 as the dashed line. The NEP for BLIP detection is plotted as the solid line in the same figure; here we have taken NEP for BLIP detection to be given as:

$$\text{NEP}_{(\text{BLIP})} = 2 \left(\frac{P_b h \nu \Delta f}{\eta} \right)^{1/2}$$

where P_b is the power incident on the face of the detector, $h\nu$ the photon energy between 8 and 12 μ , Δf the bandwidth (1 Hz), and η the efficiency including the reflection loss and that due to the absorption of the material. The absorption coefficient for our detector ($\sim 4 \text{ cm}^{-1}$) over the wavelength of interest (8 to 12 μ) was deduced by inserting a 3-mm cube of detector material behind the first limiting cold aperture and measuring the transmission. A comparison of the experimental and theoretical background limited curves shows that these detectors exhibit very little extraneous noise for backgrounds as low as about 10^{-11} W (NEP $\sim 10^{-15}$ W).

Some measurements of relative response as a function of temperature have been made with the detector field held constant at 50 V/cm. There appear to be two regions of near linear behavior, one between 4.5° and 7°K and the other between 8° and approximately 12°K with a transition between 7° and 8°K. However, for these preliminary measurements it is not possible to say if any fundamental significance should be attached to this apparent transition between 7° and 8°K. It should also be noted that this temperature variation of responsivity does not follow any of the usual theories dealing with thermal variation of the hole lifetime and mobility.

T. M. Quist
R. J. Keyes

D. MAGNETICALLY TUNED SEMICONDUCTOR LASERS FOR INFRARED HETERODYNE MEASUREMENTS

Several techniques can be used to produce two coherent beams of slightly different wavelengths for heterodyning via a square-law detector. In general, these techniques involve either a Doppler-shifted laser line or the beating of two distinct modes of a gas laser, and each has its limitations. Doppler-shifted signals require moving objects, such as a spinning wheel or a piezo-electric oscillator, but mechanical stress limitations restrict the IF frequency to 50 MHz or less.² Beating between the modes of a He-Ne gas laser have produced IF frequencies of as high as 150 MHz (Ref. 3); however, this technique is not amenable to continuous tuning over a wide range.

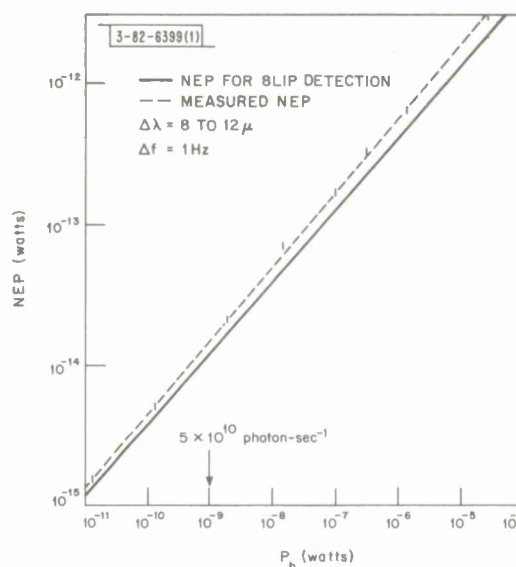


Fig. II-5. Comparison of measured noise equivalent power and BLIP detection as a function of background power for the 8- to 12- μ region.

Section II

We have performed some preliminary experiments to determine the feasibility of using a pair of semiconductor p-n junction lasers, one of which is tuned magnetically, to produce continuous IF frequencies well into the GHz range. These experiments were performed with PbSe diode lasers cooled to liquid helium temperatures in a "contact" dewar. Our primary concern is the change in laser line wavelength and intensity with diode current, temperature, and magnetic field, as well as variations from one diode laser to another. The diodes were cleaved into rectangular parallelepipeds approximately 500 μm long, with a square cross section 250 μm on edge.* The laser wavelength λ is given by the Fabry-Perot cavity equation which, neglecting dispersion, is

$$m\lambda = 2n(H)\ell \quad (1)$$

where m is an integer representing the number of half-waves between the end faces, $n(H)$ the magnetic-field-dependent index of refraction [$n(0) \approx 7.0$], and ℓ the cavity length. A mode spacing of 106.4 \AA is predicted by Eq. (1) for a PbSe laser under the above conditions – and this implies a frequency spacing between adjacent modes of 44.2 GHz. Butler and Calawa⁴ have

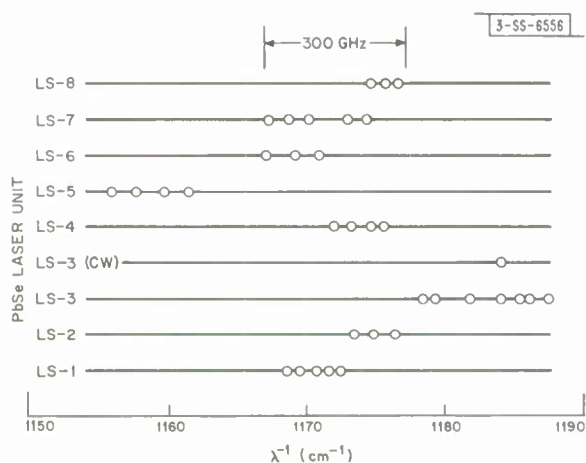


Fig. II-6. Positions of laser modes for eight PbSe diodes at liquid helium temperatures. All data represent pulsed operation, except for that point designated CW.

PbSe diodes tested. The central modes for each unit correspond roughly to the peak in the spontaneous emission. All but two of the diodes exhibited mode structure within a 300-GHz frequency range, indicating the extent to which the spontaneous emission coincided from one unit to another. Assuming an energy gap variation with temperature of $4 \times 10^{-4} \text{ eV/}^\circ\text{K}$, this spread corresponds to a temperature difference of 3°K. No attempts were made to fabricate diodes with identical cavity lengths for these preliminary measurements, so that any coincidence of the mode positions between different units is accidental at this point.

In order to prevent the simultaneous heterodyning between corresponding modes of two multi-mode lasers, one or both lasers must operate in the single-mode configuration. Moreover, CW operation is desirable in order to limit temperature transients caused by the current pulses and

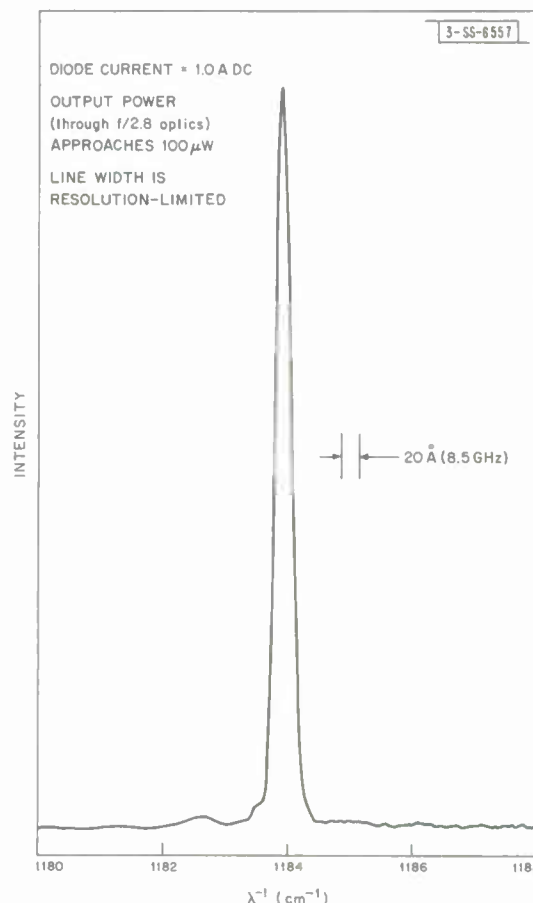
shown that the wavelength of the coherent emission from a PbSe diode laser varies with magnetic field at a rate of -14 \AA/kG , and consequently a magnetic field of 7.6 kG is sufficient to shift a laser line from one "mode position" to the adjacent one. In terms of the IF frequency, the shift is 5.82 GHz/kG, which indicates that for a frequency stability of 10 kHz the magnetic field ripple must be smaller than 1.7 G.

Equation (1) shows that any variation in n or ℓ will produce a proportionate change in λ . (It is the variation of the refractive index with magnetic field which permits continuous tuning of the laser wavelength; the magnetostriction, or variation in cavity length with magnetic field, is negligible.) Figure II-6 illustrates the positions of the dominant laser modes for the eight

* We thank F. H. Caswell of Group 85 for fabricating the PbSe laser diodes.

to simplify the IF frequency measurement. As shown in Fig. II-7, single-mode and CW operation are compatible for PbSe diode lasers. With a steady current of 1.0 A the power emanating from the dewar ($f/2.8$ optics) is almost $100\text{ }\mu\text{W}$. The measured linewidth of $20\text{ }\text{\AA}$ (8.5 GHz)

Fig. II-7. Single-mode laser emission from PbSe diode LS-3 at liquid helium temperature.



represents the resolution limit of the spectrometer under the conditions of the experiment. The diode laser represented in Fig. II-7 was the only one of the eight tested with a series resistance and laser threshold low enough to permit CW operation. We are presently fabricating diode lasers which will have properties tailored to the actual heterodyne measurements.

E. D. Hinkley

E. EXCESS NOISE IN PHOTOCONDUCTIVE Ge:Cu DETECTORS

Optical heterodyne detection with photoconductive detectors theoretically yields a signal-to-noise power ratio of $\eta P_s / 2h\nu B$. Previous experiments on photoconductive Ge:Cu at $10.6\text{ }\mu$ have come within a factor of 3 of this ratio.⁵ The absolute values of signal and noise power, however, were larger than would be expected from the measured responsivity. Also a rising low frequency noise spectrum was observed in some of these detectors in use in a prototype laser radar system. Measurements have been under taken to determine the source of these anomalous characteristics.

Section II

The photocurrent noise spectrum of a photoconductor illuminated with either coherent or thermal radiation of sufficiently low intensity⁶ can be shown to be $(4I_0 e \tau / T) / (1 + \omega^2 \tau^2)$ (one-sided spectrum) where I_0 is the average current, e is the electronic charge, τ is the carrier lifetime, and T the transit time across the detector. This expression assumes that trapping is absent and that the random generation and recombination of charge pairs is the only noise source.

The detectors studied (supplied by T. M. Quist of this group) measured $5 \times 5 \times 3$ mm with the radiation incident on the square face. The starting material measured 41 ohm-cm. Copper concentration after diffusion was $7 \times 10^{15} \text{ cm}^{-3}$ and the measured responsivity was 0.2 A/W at 80 V/cm. Assuming a quantum efficiency of 1/2, the calculated half-power frequency, $1/2\pi\tau$, was about 10 MHz.

Noise spectra from these detectors have been measured using both black body and laser illumination at 10.6μ . In both cases $1/f$ noise* appeared well below the half-power frequency of the detector. In the laser case, however, the noise power was appreciably larger than that for equivalent black body illumination (a factor of approximately 4 for 10 mW optical power input). Subsequent measurement of noise density in the $1/f$ region as a function of incident power showed its dependence on I_0 to be approximately $I_0^{1.2}$ for the black body and $I_0^{1.9}$ for the laser. These values are commensurate with the expected dependences of G-R noise and amplitude fluctuations of the input, respectively.

It is clear that there is a substantial contribution to the excess noise from laser amplitude fluctuations. The source of the $1/f$ noise in the black body measurements is more obscure. Our current speculation is that radiation induced minority carrier injection is occurring at the contacts. Since the short majority carrier lifetimes in these detectors are achieved by charge compensation, one would expect the minority carrier lifetimes to be appreciably longer. This mechanism would account for both the $1/f$ noise and excess noise at low frequencies noted in Ref. 5.

A. H. M. Ross

REFERENCES

1. Solid State Research Report, Lincoln Laboratory, M. I. T. (1967:4).
2. See, for example, M. C. Teich, Proc. IEEE 56, 37 (1968).
3. James T. Yardley and C. Bradley Moore, Appl. Phys. Lett. 7, 311 (1965).
4. J. F. Butler and A. R. Calawa, Physics of Quantum Electronics (McGraw-Hill, New York, 1966), p. 458.
5. M. C. Teich, R. J. Keyes, and R. H. Kingston, Appl. Phys. Letters 9, 357 (1966).
6. L. Mandel, Proc. Phys. Soc. (London) 72, 1037 (1958).

* We use the " $1/f$ noise" designation merely to describe the general character of the spectrum. It has not been verified that the dependence is $1/f$.

III. MATERIALS RESEARCH

A. AN OPEN TUBE REACTOR FOR PREPARING COMPOUNDS WITH VOLATILE CONSTITUENTS

A great number of inorganic compounds are prepared by reacting the elements in closed silica ampoules. However, for compounds of sufficiently volatile elements (those from Groups II, V, and VI of the periodic table), the heat of reaction frequently causes explosions, unless the materials are heated very slowly in small quantities. To overcome this difficulty, an open tube reactor has been constructed for synthesizing such compounds at essentially constant pressure, by repeatedly dropping small amounts of the reaction mixture into a crucible hot enough to produce rapid vaporization and reaction. Use of this apparatus makes it possible to produce such compounds as ZnTe and ZeSe at the rate of 100 to 300 g/h.

A schematic diagram of the reactor is shown in Fig. III-1. Its principal parts, which are made of fused silica, are a vertical reactor tube about 5 cm in diameter and 35 cm long, a crucible which rests on the bottom of this tube, an L-shaped addition tube which fits into the top of the reactor tube, and a piston which is placed in the horizontal part of the addition tube. Silicone O-rings are used to permit insertion of the addition tube into the reactor tube and motion of the piston inside the addition tube. Titanium-gettered helium gas enters the system through an inlet in the addition tube and leaves through outlets in the addition and reactor tubes. The lower end of the reactor tube is placed just below the center of a resistance-heated muffle furnace capable of operating up to 1100°C.

A charge of stoichiometric composition is prepared by mixing the elements in the form of irregular pieces with dimensions of 5 to 10 mm. This coarse mixture is placed in the horizontal part of the addition tube, after which a plug of quartz wool and the piston are inserted. The system is then flushed with helium. Initially the outlet in the addition tube is open, so that helium passes over the charge. Then an O-ring is moved to close this outlet, and during the rest of the run all the helium passes through the outlet in the reactor tube, and then through a bubbler which maintains the gas pressure at slightly above one atmosphere. The muffle furnace is heated to the operating temperature.

To initiate synthesis, the piston is slowly pushed into the addition tube, causing small quantities of the charge to fall at irregular intervals into the reactor tube, where they vaporize and

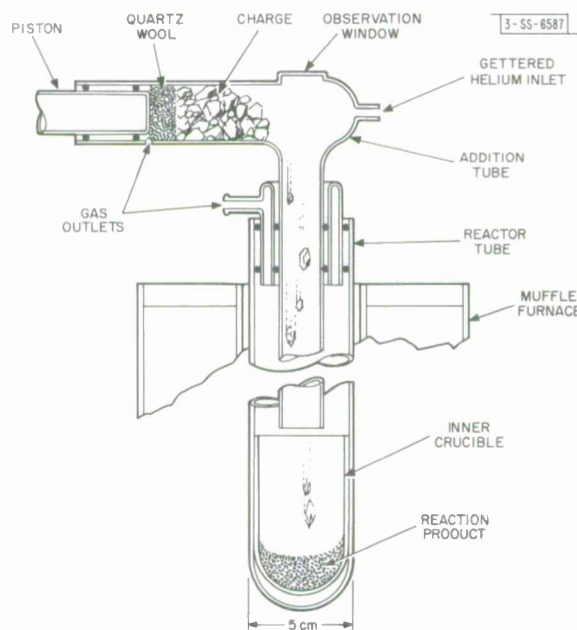


Fig. III-1. Open tube reactor for preparing compounds with volatile constituents.

Section III

react. Small flashes of light produced by the repeated reactions can be observed through the roiling vapor clouds by means of an observation window in the addition tube. The progress of the reaction can also be monitored by observing changes in the rate of gas bubbling and in the behavior of the furnace temperature controller, which reflect variations in the pressure and temperature in the system. Typically, a charge of 150 to 300 g can be reacted in an hour or less without danger of explosion.

Because the charge is such a coarse mixture of the elements, the composition of each small portion dropped into the reactor is non-stoichiometric. A considerable loss of unreacted material, due to volatilization and subsequent condensation on the cooler parts of the reactor, might therefore be expected. However, the amount of lost material is usually less than 2 percent of the total charge. It seems probable that the vapor produced by a temporary excess of one element, because it is more dense than helium gas, remains in the bottom of the reactor until the stoichiometry is restored by the arrival of an additional portion of the charge. A volume of 250 cm^3 at 1000°C can store about 0.3 g of a vapor whose molecular weight is 100.

In most cases, after the reaction is completed the product is allowed to "soak" at the reaction temperature under helium, in order to increase its crystallinity and remove as much unreacted material as possible. A dense, homogeneous boule is generally formed in the bottom of the crucible. In many cases the boule can be removed easily at the conclusion of the run, but for materials which wet quartz it cannot be removed without breaking the crucible.

The following compounds and pseudo-binary alloys have been synthesized to date: ZnTe , ZnSe , $\text{ZnTe}_{1-x}\text{Se}_x$ ($x = 0.2, 0.8$), $\text{Zn}_{1-x}\text{Mg}_x\text{Te}$ ($x = 0.1, 0.2$), $\text{Cd}_{1-x}\text{Mg}_x\text{Te}$ ($0.1 \leq x \leq 0.7$), and GaS . In most cases the reaction temperature was between 1000° and 1100°C . For very high reaction rates, the temperature should be above the boiling point of at least one of the reactants. Satisfactory ZnTe runs have been made between 800° and 1150°C , although the boule made at 800°C appears to contain unreacted Te , which boils at 990°C . To prepare $\text{Cd}_{1-x}\text{Mg}_x\text{Te}$ alloys, it was necessary to cool the reactor quickly after synthesis, since it was found that soaking at the reaction temperature for 24 hours caused all the CdTe to evaporate from the boule. The reaction temperature for GaS had to be above 965°C , the melting point of the compound, to prevent forming a layer of solid GaS which inhibits further reaction. The reaction product contained Ga which separated as a second phase on cooling and could be leached out with HCl .

T. B. Reed
W. J. LaFleur

B. CRYSTAL GROWTH FROM THE VAPOR PHASE BY FORCED CONVECTION

Single crystals up to 1 cm on a side have been grown by sublimation and condensation of several semiconducting compounds and alloys. Forced convection in an open tube, using helium, hydrogen, or a helium-hydrogen mixture as the carrier gas, is employed to obtain vapor transport rates higher than those which can be achieved by diffusion or natural convection in closed systems.

The growth apparatus consists of a fused silica tube about 90 cm long which is placed in a horizontal resistance-heated furnace. The apparatus and temperature profile are shown schematically in Fig. III-2. A coarsely pulverized charge of the compound or alloy is placed in the

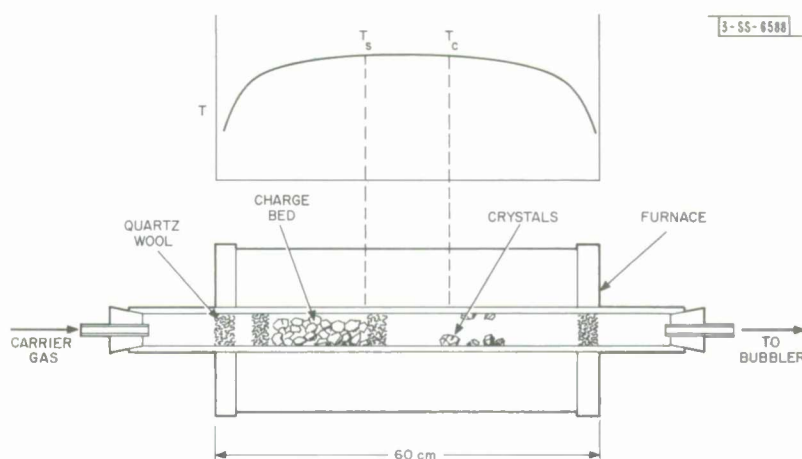


Fig. III-2. Open tube apparatus for crystal growth by forced convection.

tube between two quartz wool plugs. Tubes of 2.5- and 5-cm o.d. have been used. The diameter is chosen so that the amount of charge used will form a bed 10 to 15 cm long which fills the entire cross section of the tube. The carrier gas enters the tube from the left in Fig. III-2, passes through the charge bed and the crystal growth region, and leaves at the right. If the gas velocity is low enough, the gas becomes saturated with vapor at T_s , the temperature at the end of the bed. (In the case of ZnTe, measurements of the weight lost by the bed have shown that saturation is attained at the gas velocities used in crystal growth.) The slight increase in temperature between the beginning and end of the bed facilitates the uniform removal of material from all regions of the bed, thus reducing channeling and plugging. Crystals begin to grow at a temperature T_c slightly below T_s and deposit uniformly over a condensation region about 20 cm long. Although T_s and T_c have not been measured accurately, temperature profiles taken along the axis and at the wall of the tube suggest that the difference between these two temperatures is less than 10°C . The temperature reaches a maximum at a point between the end of the charge bed and the beginning of the condensation region, causing desaturation of the carrier gas and decreasing the likelihood of constitutional supercooling in the growth of crystals at T_c .

Crystals of Cd_3As_2 , PbTe , SnTe , $\text{Pb}_{1-x}\text{Sn}_x\text{Te}$ alloys, ZnTe , and $\text{ZnTe}_{1-x}\text{Se}_x$ alloys have been grown in the forced convection apparatus. The growth conditions used and the approximate dimensions of the largest crystals obtained are listed for each material in Table III-1. Over the range of carrier gas velocities employed, there is no obvious correlation between velocity and crystal size. Two of the largest ZnTe crystals are shown in Fig. III-3. Most of the ZnTe crystals are transparent, distinctly orange (whereas impure crystals are frequently red), and exhibit less intense red photoluminescence due to oxygen substituted for tellurium than the charge from which they are grown.

Fractionation effects due to differences in volatility are generally observed in the growth experiments. At the conclusion of most runs, deposits of impurities less volatile than the grown crystals are left behind in the original location of the charge bed, and frequently deposits of more volatile impurities are found beyond the crystal growth region. In the growth of alloy crystals, these purification effects are accompanied by segregation effects, which cause the

TABLE III-1 GROWTH CONDITIONS AND CRYSTAL DIMENSIONS IN FORCED CONVECTION EXPERIMENTS				
Material	Temperature of Charge Bed (°C)	Carrier Gas	Gas Flow (cm ³ /min-cm ²)	Largest Crystals (mm)
Cd ₃ As ₂	550 to 625	H ₂ , He	80 to 500	5 × 5 × 1
PbTe	890	H ₂ , He	80 to 500	10 × 10 × 2
SnTe	790	He	100	1 × 1 × 1
Pb _{1-x} Sn _x Te	850	H ₂ , He	50 to 200	3 × 5 × 5
ZnTe	1000 to 1075	H ₂ , He, He(15% H ₂)	20 to 90	10 × 10 × 5
ZnTe _{0.8} Se _{0.2}	1000	He	90	5 × 5 × 4

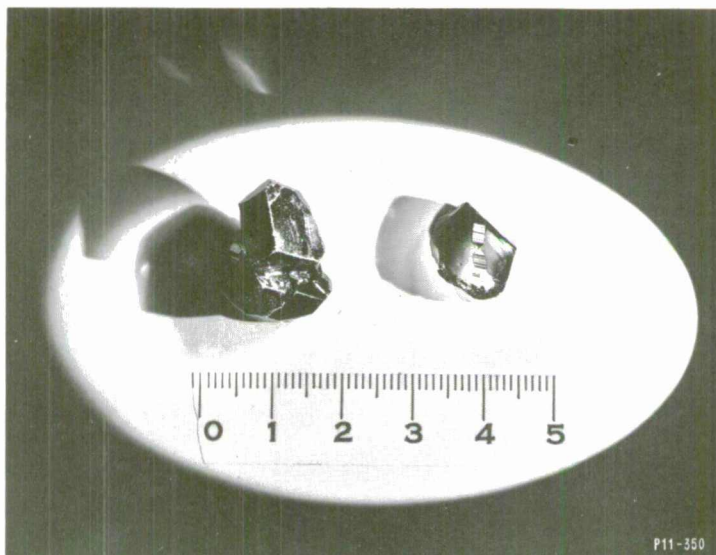


Fig. III-3. Crystals of ZnTe grown by forced convection.

TABLE III-2
SEGREGATION IN CRYSTAL GROWTH OF ALLOYS

	$\text{Pb}_{1-x}\text{Sn}_x\text{Te}$		$\text{ZnTe}_{1-x}\text{Se}_x$	
	a_o (Å)	x	a_o (Å)	x
Charge				
Starting composition		0.20		0.20
First to evaporate	6.419	0.17	5.707	0.91
Last to evaporate (at T_s)	6.411	0.23	6.010	0.21
Crystals				
First to condense (at T_c)	6.400	0.31	6.078	0.058
Last to condense	6.386	0.41	6.101	0.004

composition of the grown crystals to vary as a function of distance along the tube. The composition of the untransported portion of the charge also varies with distance. Data on the composition changes observed in the growth of $\text{Pb}_{1-x}\text{Sn}_x\text{Te}$ and $\text{ZnTe}_{1-x}\text{Se}_x$ alloys are given in Table III-2. The composition values listed were obtained from lattice parameter measurements by assuming that Vegard's law is valid for both pseudo-binary systems.

T. B. Reed
W. J. LaFleur

C. PARTIAL PRESSURES AND THERMODYNAMIC PROPERTIES IN THE Si-Te SYSTEM

The optical density between 2400 and 7000 Å of the vapor in equilibrium with Si-Te samples containing between 10 and 100 atomic percent Te has been measured for sample temperatures between 500 and 940°C. Absorption spectra due to $\text{Te}_2(\text{g})$ and $\text{SiTe}(\text{g})$ were observed. The partial pressures of $\text{Te}_2(\text{g})$, p_{Te_2} , were obtained from the optical densities at 4357, 5000, and/or 5500 Å, where $\text{SiTe}(\text{g})$ does not absorb, using calibration curves determined in experiments on pure Te. The values of p_{Te_2} on a logarithmic scale are plotted in Fig. III-4 as a function of reciprocal absolute sample temperature. These results show that $\text{Si}_2\text{Te}_3(\text{c})$ is the only solid compound in the Si-Te system, as reported by Bailey,¹ and that its homogeneity range falls within outer limits of 59.45 and 60.50 atomic percent Te and ends at a peritectic temperature of 892°C.

X-ray powder diffraction patterns indicate that the $\text{Si}_2\text{Te}_3(\text{c})$ phase is the same as the one previously identified by some authors as $\text{SiTe}_2(\text{c})$. At 892°C, p_{Te_2} in equilibrium with $\text{Si}_2\text{Te}_3(\text{c})$ is 7×10^{-2} atmosphere. Below the peritectic temperature, p_{Te_2} increases markedly with increasing Te content across the homogeneity range of $\text{Si}_2\text{Te}_3(\text{c})$. At 604°C, for example,

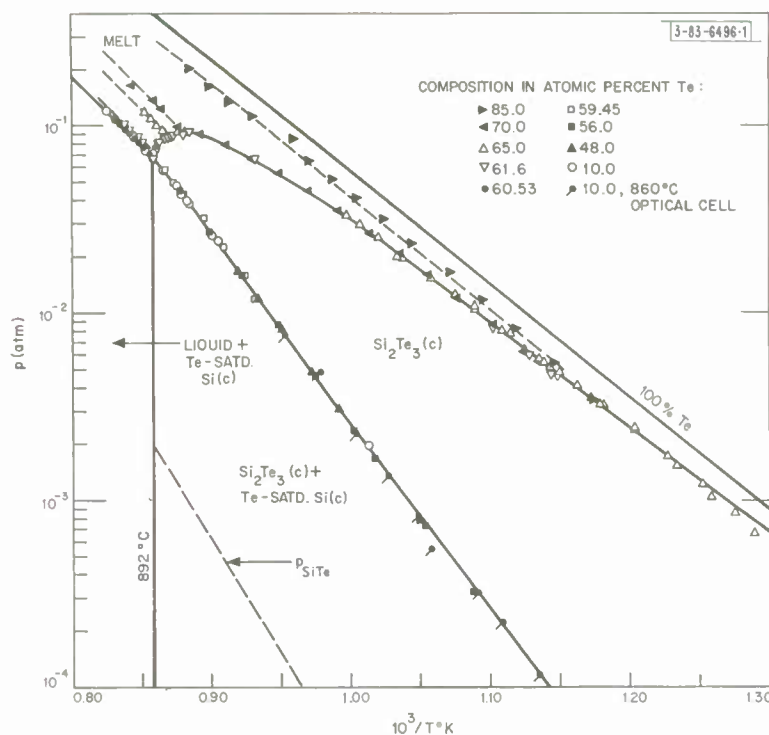


Fig. III-4. Partial pressures in the Si-Te system as a function of reciprocal absolute sample temperature.

p_{Te_2} is 10^{-4} and 5.4×10^{-3} atmosphere for Si-saturated and Te-saturated $\text{Si}_2\text{Te}_3(\text{c})$, respectively. From the values of p_{Te_2} , together with published data for the vapor pressure of $\text{Te}(\ell)$, the standard Gibbs free energy change for the reaction $0.4 \text{ Si}(\text{c}) + 0.6 \text{ Te}(\ell) \rightarrow \text{Si}_{0.4}\text{Te}_{0.6}(\text{c})$ is found to be $\Delta G_f^0 = -5.754 + 3.904(10^{-3}) T$ kcal/g-atom between 604° and 892°C .

The net optical densities for $\text{SiTe}(\text{g})$ at 2708 and 2893 \AA , which were obtained by subtracting the optical densities of $\text{Te}_2(\text{g})$ from the measured densities at these wavelengths, were found to be in constant ratio to each other. Values of p_{SiTe} cannot be obtained directly from the optical densities because no calibration data are available. However, if it is assumed that p_{SiTe} is proportional to the optical density (i. e., that Beer's law is obeyed), the standard heat of formation for the reaction $\text{Si}(\text{g}) + \frac{1}{2} \text{Te}_2(\text{g}) \rightarrow \text{SiTe}(\text{g})$ is found to be $\Delta H_f^0 = -74.83$ kcal/mol. This value, combined with published data for $\text{Si}(\text{g})$ and $\text{Te}_2(\text{g})$ and theoretical calculations of $(H_T^0 - H_O^0)$ and S_T^0 for $\text{SiTe}(\text{g})$, gives $D_O^0 = 99.4$ kcal/mol for the dissociation energy of $\text{SiTe}(\text{g})$ and gives values for p_{SiTe} which are consistent with the assumption that $\text{SiTe}(\text{g})$ obeys Beer's law at 2708 and 2893 \AA . The values of p_{SiTe} in equilibrium with Si-saturated $\text{Si}_2\text{Te}_3(\text{c})$ are plotted as the lowest dashed line in Fig. III-4 as a function of reciprocal absolute sample temperature. From these values, together with the partial pressures of $\text{Si}(\text{g})$ and $\text{Te}_2(\text{g})$, the standard Gibbs free energy of formation for $\text{SiTe}(\text{g})$ is found to be $\Delta G_f^0 = -74.86 + 15.77(10^{-3}) T$ kcal/mol between 700 and 892°C .

R. F. Brebrick

D. HIGH-PRESSURE PHASE DIAGRAM OF InSb

A tentative high-pressure phase diagram for InSb was presented in a previous issue of this quarterly report.² In addition to the liquid phase and cubic InSb-I phase stable at atmospheric pressure, that diagram includes three high-pressure phases: tetragonal InSb-II, InSb-III of unknown structure, and an orthorhombic phase first observed by Kasper and Brandhorst.³ A new pressure-temperature diagram, which is shown in Fig. III-5, has now been constructed on the basis of additional superconducting transition temperature (T_c) and x-ray diffraction measurements on samples of the high-pressure phases prepared at various pressures and temperatures. The results of these measurements, which confirm the main features of the earlier diagram, establish accurate phase boundaries between InSb-II and InSb-III, and between InSb-II and the orthorhombic phase (which has been designated as InSb-IV). In addition, they locate the III-IV phase boundary more accurately, show that InSb-III has a hexagonal structure, and yield lattice parameters for all three high-pressure phases.

No great difficulty was encountered in establishing the II-III phase boundary, since the temperatures along this boundary are high enough for equilibrium to be established within a few days, in spite of the effect of high pressure in reducing self-diffusion rates. It was considerably more difficult to locate the II-IV boundary, because the time required to achieve equilibrium is much longer at the lower temperatures (maximum of 175°C) along this boundary. To be sure that equilibrium was attained, samples were prepared by crossing the boundary in both directions, and annealing times of 10 to 21 days were employed. Samples which were initially single-phase InSb-II or InSb-IV were found to contain both phases after annealing up to 10 days at 25 kbars and 100°C. Therefore the phase boundary has been drawn through this P-T point. The

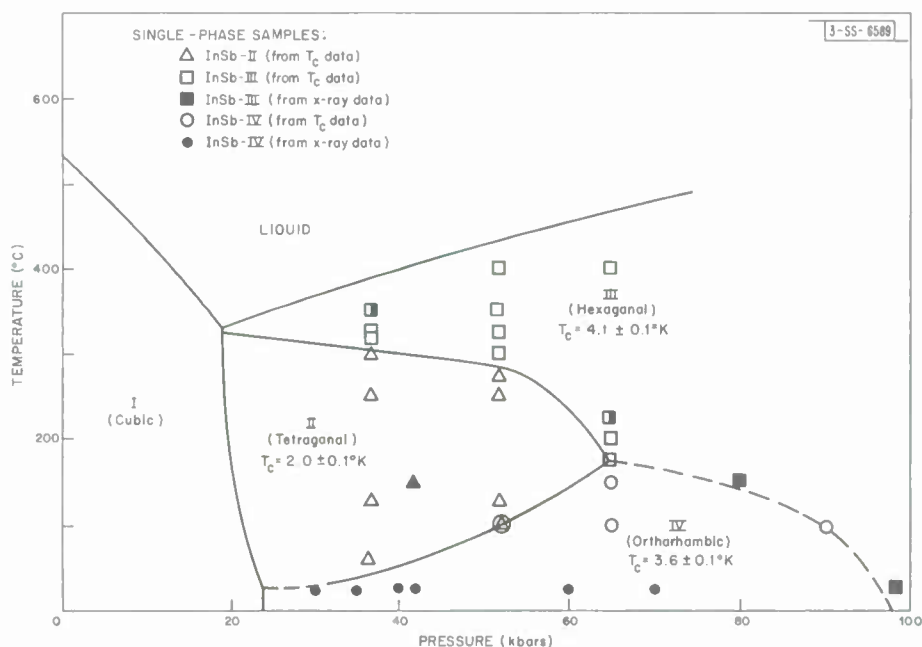


Fig. III-5. High-pressure phase diagram of InSb.

Section III

TABLE III-3
X-RAY DIFFRACTION DATA FOR HIGH-PRESSURE PHASES OF InSb

InSb-II at 26 kbars* Tetragonal $a = 5.862 \text{ \AA}$, $c = 3.105 \text{ \AA}$ $\rho_{\text{calc}} = 7.3 \text{ g/cm}^3$				InSb-IV at ~70 kbars† Orthorhombic $a = 2.921 \text{ \AA}$, $b = 5.532 \text{ \AA}$, $c = 3.093 \text{ \AA}$; $\rho_{\text{calc}} = 7.9 \text{ g/cm}^3$				InSb-III at ~90 kbars† Hexagonal $a = 6.099 \text{ \AA}$, $c = 5.708 \text{ \AA}$ $\rho_{\text{calc}} = 8.5 \text{ g/cm}^3$			
hkl	$d_{\text{exp}} (\text{\AA})$	$d_{\text{calc}} (\text{\AA})$	I_{obs}	hkl	$d_{\text{exp}} (\text{\AA})$	$d_{\text{calc}} (\text{\AA})$	I_{obs}	hkl	$d_{\text{exp}} (\text{\AA})$	$d_{\text{calc}} (\text{\AA})$	I_{obs}
200	2.946	2.931	s+	001	3.061	3.058	vw	00.2	2.864	2.854	s+
101	2.753	2.742	s	100	2.918	2.921	s+	20.0	2.662	2.641	s
211	2.003	2.005	s	020	2.763	2.766	s-	20.1	2.420	2.396	vvw
311	1.603	1.592	m-	011	2.652	2.649	s	20.2	1.943	1.939	s
400	1.467	1.467	m	101	2.100	2.101	w	22.0	1.526	1.526	m-
410	1.407	1.423	vw	120	2.012	2.012	s	00.4	1.425	1.425	w
202	1.379	1.372	w	111	1.952	1.950	s	22.2	1.349	1.346	m
411	1.292	1.292	m	030	1.861	1.860	w	20.4	1.251	1.254	m
222	1.244	1.242	vw	121	1.674	1.675	m	40.2	1.200	1.199	vw
511	1.073	1.076	vw	031	1.570	1.580	s-	20.5		1.047	w
								22.4	1.042	1.041	
								50.1		1.040	
				002	1.520	1.521	w	42.0	0.997	0.999	w
								50.2		0.992	
				200	1.450	1.450	s-				
				040	1.391	1.392	s-				
				102	1.346	1.346	w				
				201	1.315	1.308	vvw				
				220	1.282	1.286	m				

* NaCl used as internal calibrant.

† Based on experience with calibration runs.

point at 65 kbars and 175°C has been adopted as the II-III-IV triple point, since different samples annealed under these nominal conditions had T_c values characteristic of either InSb-II, InSb-III, or InSb-IV, and in some cases had double transitions indicating the presence of two phases. It is assumed that the variation in results was due to small differences between the actual and measured annealing pressures and temperatures.

At room temperature, x-ray data show that InSb-I is transformed directly into InSb-IV with increasing pressure, if the pressure is applied slowly enough above 20 kbars. (A rate of 0.5 kbar/h is sufficiently slow.) Therefore the I-II-IV triple point has been located just above room temperature in Fig. III-5. However, McWhan and Marezio⁴ found that InSb-II was obtained at room temperature if the pressure was increased to 40 kbars in a sufficiently short time (in their experiments, one-half minute). This apparently inconsistent observation, which has been duplicated in our experiments, can be explained by the shallow slope of the II-IV phase boundary, together with the fact that the transformation of InSb-II into InSb-IV at room temperature proceeds very slowly. If the rapid application of pressure causes the sample temperature to rise by the small amount necessary to cross the II-IV boundary, InSb-II will be formed as the stable phase, and at 40 kbars it will not transform into InSb-IV even after the sample temperature returns to room temperature.

The III-IV phase boundary is not well defined by the available data. The pressure values for the single-phase InSb-III samples shown in Fig. III-5 at room temperature and at 150°C are somewhat uncertain. The data for these samples were obtained with diamond-anvil squeezers, and the pressures were estimated from separate calibration runs, rather than by using an internal standard. The single-phase InSb-IV sample shown at 90 kbars and 100°C was identified by T_c measurements after the sample had been annealed under these conditions and then cooled to liquid nitrogen temperature before releasing the pressure. This P-T point might actually lie inside the InSb-III stability field, since it is not certain that InSb-III prepared at 90 kbars can be retained as a metastable phase at atmospheric pressure by the quenching procedure used. Resistivity measurements between 70 and 100 kbars were also made in an attempt to locate the III-IV boundary at room temperature. However, this attempt was unsuccessful, since no discontinuity was observed, although Minomura, *et al.*⁵ have reported one at about 80 kbars.

Table III-3 lists room temperature x-ray diffraction data for the three high-pressure phases of InSb, together with the structures and lattice parameters based on these data. The data for InSb-II and InSb-IV confirm the earlier assignments of tetragonal² and orthorhombic^{3,4} structures, respectively. The results for InSb-III show that this phase is hexagonal. Single-phase patterns of InSb-III were consistently obtained at room temperature by gradually increasing the pressure on the sample until the entire sequence of patterns for InSb-I, InSb-II, InSb-IV, and InSb-III was complete. A single-phase pattern for InSb-III could also be obtained by raising the temperature to 150°C at a pressure which gave primarily InSb-IV at room temperature. Due to the pressure gradients across the sample in the x-ray camera, patterns containing lines of two adjacent phases were frequently obtained. In determining the correct structure of InSb-III, it was necessary to obtain a pattern which did not also contain lines due to InSb-IV, since it was found that such a mixed pattern could be indexed on an orthorhombic cell with large lattice parameters.

Section III

There is considerable similarity between the diffraction lines of InSb-III and InSb-II. It is possible to index InSb-III as tetragonal by assuming the same indices as for InSb-II, but the fit between observed and calculated d-values is much better for the hexagonal indexing. There is no ambiguity between the patterns for InSb-II and InSb-IV. The appearance of the third strong line for the orthorhombic triplet is clear evidence that InSb-IV is present.

M. D. Banus
Mary C. Lavine

E. HIGH-PRESSURE PEROVSKITE PHASE OF RbNiF_3

The phase of RbNiF_3 stable at atmospheric pressure, which is one of the few transparent ferrimagnetic compounds,⁶ has the hexagonal BaTiO_3 structure with $a = 5.842 \text{ \AA}$ and $c = 14.311 \text{ \AA}$. By subjecting this phase to a pressure of 65 kbars at 600°C , it has been transformed into a high-pressure phase with the cubic perovskite structure. All x-ray diffraction lines for the new phase can be indexed on the basis of a primitive cubic cell with $a = 4.07 \text{ \AA}$. There is some line broadening at high diffraction angles, which indicates a possible deviation from cubic symmetry.

A magnetic study of the high-pressure phase shows it to be antiferromagnetic, with a broad transition at a Néel temperature (T_N) of about 285°K . The magnetic susceptibility at 4.2° and 300°K varies linearly with applied field up to 17 kOe, the highest field investigated. The atmospheric pressure phase of KNiF_3 also has the perovskite structure ($a = 4.015 \text{ \AA}$) and is antiferromagnetic ($T_N = 275^\circ\text{K}$).⁷

J. M. Longo
J. A. Kafalas
D. A. Batson

F. CaCrO_3 - A NEW ANTIFERROMAGNETIC PEROVSKITE

A new perovskite, CaCrO_3 , has been prepared by reacting a stoichiometric mixture of CaO and CrO_2 in a gold capsule at a pressure of 65 kbars and temperature of 700°C . It is very important that the reactants be completely dry and thoroughly mixed. Mixing, which was accomplished by grinding with an agate mortar and pestle, and all other steps in sample preparation were carried out in a nitrogen-filled glove bag. The product always contained a trace of Cr_2O_3 .

The compound has the orthorhombically distorted perovskite structure with $a = 5.28 \text{ \AA}$, $b = 5.31 \text{ \AA}$, and $c = 7.48 \text{ \AA}$. It is antiferromagnetic, with Néel temperature $T_N = 90^\circ\text{K}$. At T_N , there is a sudden increase in susceptibility due to the onset of parasitic ferromagnetism. In measurements of the pressure dependence of T_N , as determined from the increase in susceptibility, it was found that up to 6 kbars $dT_N/dP = -0.23^\circ\text{K/kbar}$.

The resistivity of a very dense, thin cylinder of CaCrO_3 was measured by the van der Pauw method. The relatively high values of $1.4 \times 10^4 \text{ ohm-cm}$ at 300°K and $1.1 \times 10^6 \text{ ohm-cm}$ at 77°K indicate that the compound is a semiconductor rather than a metal.

Two features are significant about the properties of CaCrO_3 : (1) According to the T-b electronic phase diagram recently presented,⁸ the negative pressure coefficient of T_N indicates that the transfer energy b , which is a measure of the Cr-O-Cr interactions, lies in the interval $b_c < b < b_m$, corresponding to spontaneous band antiferromagnetism. This property is consistent with the variation in physical properties exhibited by other ABO_3 perovskites, as listed in

TABLE III-4 PROPERTIES OF ABO_3 PEROVSKITES WITH B-CATION d-ELECTRON CONFIGURATION t_{2g}^2			
Compound	Structure*	Transport	Magnetic
$BoMoO_3$	C	Metallic	Pauli paramagnetic
$SrMoO_3$	C	Metallic	Pauli paramagnetic
$SrCrO_3$	C	Metallic	Pauli paramagnetic
$CoCrO_3$	O	Semiconductor	$T_N = 90^\circ K$
$PbCrO_3$	C	Semiconductor	$T_N = 240^\circ K$
$LaVO_3$	$O' \xrightarrow{T_N} O$	Semiconductor	$T_N = 137^\circ K$
YVO_3	$? \xrightarrow{T_N} O$	Semiconductor	$T_N = 73^\circ K$
* C = Cubic, O = Orthorhombic $a < c/\sqrt{2}$, O' = Orthorhombic $c/\sqrt{2} < a$.			

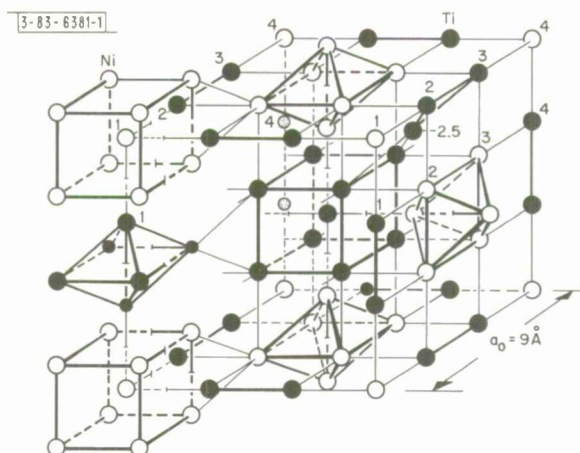
Table III-4. (2) Parasitic ferromagnetism is commonly encountered in antiferromagnetic perovskites which have the orthorhombic structure and localized d-electrons ($b < b_c$). The small spin canting is primarily due to antisymmetric superexchange. Since $CaCrO_3$ and $CaRuO_3$, which apparently have collective d-electrons, also exhibit parasitic ferromagnetism, an adequate microscopic model for collective-electron exchange must include an antisymmetric term.

J. M. Longo J. B. Goodenough
J. A. Kafalas D. A. Batson

G. LIKE-ATOM CLUSTER FORMATION AND ELASTIC MEMORY IN TiNi

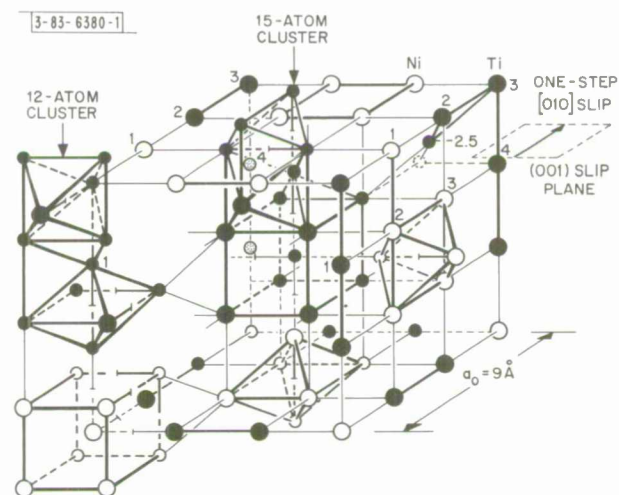
Equiatomic TiNi undergoes two transitions with increasing temperature. In the range $400 < T < 700^\circ C$ there is an order-disorder transition, the low-temperature phase having a complex cubic unit cell containing 54 atoms, the b. c. c. cell edge being enlarged by a factor of three (from 3 to 9 Å). At a lower temperature T_t , there is a first-order, diffusionless transition.⁹ T_t varies with composition; the maximum value is $166^\circ C$ for the stoichiometric compound. This "martensitic" transition exhibits three significant features: (1) The structure remains cubic with the same tripled cell edge, but atomic displacements take place within the cell. (2) TiNi is ductile and soft at $T < T_t$; it is brittle and hard at $T > T_t$. (3) TiNi exhibits an "elastic memory": a wire or sheet that has been deformed at $T < T_t$ spontaneously regains its original shape when heated to $T > T_t$.

An explanation of these properties is provided by the following model: (1) Because of the large separation of Ti and Ni in the first long series of the periodic table, d-electron bonding



BELOW T_t THERE IS A CONTRACTION (ALONG HEAVY LINES) OF THE NEAREST-NEIGHBOR SPACING WITHIN THE TWO TYPES OF LIKE-ATOM CLUSTERS AND AN EXPANSION OF THIS SPACING BETWEEN CLUSTERS (ALONG LIGHT LINES). ATOMS AT CENTERS OF NINE-ATOM CUBES (000 AND $1/2, 1/2, 1/2$) STAY FIXED, EXCEPT FOR A SMALL CHANGE IN CELL SIZE THROUGH THE FIRST-ORDER TRANSITION.

Fig. III-6. Proposed structure for ordered TiNi above the martensitic transition temperature T_t .



ATOMS OF THE (010) PLANES THAT ARE MARKED 1-1, 2-2, 3-3, AND 4-4 IN FIG. III-6 ARE LABELED SIMILARLY HERE. THE COMPLETE ATOMIC CONFIGURATION CAN BE GENERATED USING FIG. III-6.

Fig. III-7. Illustration of the 12-atom and 15-atom clusters that form across the slip plane after one-jump slip in an [010] direction on the (001) slip plane indicated. Similar Ni clusters are also formed.

is more stable for like near neighbors (n.n), whereas s-electron bonding is more stable for unlike n.n. Whereas two separate phases would optimize d-electron bonding and the CsCl type order would optimize s-electron bonding, the tripled unit cell indicates a compromise gives the most stable total bonding. This reasoning leads to the proposed ordered structure for $T > T_t$ shown in Fig. III-6, which contains two atoms with only like n.n. and 52 atoms with four like and four unlike n.n. Since the structure is cubic, the complete unit cell can be generated from the atoms shown. (2) Below T_t , like atoms form nine-atom and six-atom clusters via a contraction along the heavy lines in Fig. III-6. Such cluster formation is known to occur in several transition metal compounds having narrow d bands.¹⁰ Whereas d-bonding between like n.n. forms two interpenetrating, three-dimensional arrays at $T > T_t$, it forms only molecular bonding within clusters at $T < T_t$. Therefore the structure is ductile at $T < T_t$, where there is only s bonding between clusters; but brittle and hard at $T > T_t$, where there is three-dimensional, directional d bonding. (3) At $T < T_t$, only one-jump slip occurs on any one (001) plane. After one jump, six-atom and nine-atom clusters of like atoms become juxtaposed to form twelve-atom and fifteen-atom clusters across the slip plane, as shown in Fig. III-7. Because there is strong d-electron bonding within these larger clusters, further slip occurs at a neighboring (001) slip plane. Thus deformation occurs as successive one-jump slip rather than as many-jump slip on a single plane. Further, with a cell edge of 9 \AA , it is energetically more favorable for the structure to reconstitute itself at $T > T_t$ by returning one jump to its original position on each slip plane than to slip two jumps more. Thus an "elastic memory" effect is a natural consequence of the model.

J. B. Goodenough

REFERENCES

1. L.G. Bailey, J. Phys. Chem. Solids 27, 1593 (1966).
2. Solid State Research Report, Lincoln Laboratory, M.I.T. (1967:1), DDC 651065, p. 24.
3. J.S. Kasper and H. Brandhorst, J. Chem. Phys. 41, 3768 (1964).
4. D.B. McWhan and M. Marezio, J. Chem. Phys. 45, 2508 (1966).
5. S. Minomura, B. Okai, H. Nagasaki, and S. Tanuma, Phys. Letters 21, 272 (1966).
6. M. Shafer, T. McGuire, B. Argyle, and G. Fans, Appl. Phys. Letters 10, 202 (1967).
7. K. Hirakawa, K. Hirakawa, and T. Hashimoto, J. Phys. Soc. Japan 15, 2063 (1960).
8. Solid State Research Report, Lincoln Laboratory, M.I.T. (1967:3), DDC 661275.
9. F.E. Wang, W.J. Buehler, and S.J. Pickart, J. Appl. Phys. 36, 3232 (1965).
10. J.B. Goodenough, Czech. J. Phys. B-17, 304 (1967); Mat. Res. Bull. 2, 37 and 165 (1967).

IV. PHYSICS OF SOLIDS

A. ELECTRONIC BAND STRUCTURE

1. Excitons in Germanium over a Wide Range of Magnetic Fields

The observation of exciton fine structure in the interband magnetoabsorption of InSb and germanium has shown the need, and has provided the means, for taking the exciton interaction into account in analyzing the magnetoabsorption spectra of these materials.¹ The observed fine structure also provides a means of studying the behavior of an exciton in a high magnetic field. We are obtaining detailed experimental results for the direct transition in germanium at helium temperatures and magnetic fields up to 80 kG. The results at the higher magnetic fields are obtained using a superconducting solenoid. Detailed fine structure is observed in the peak corresponding to transitions involving the $n = 0$ Landau level in the conduction band. Fine structure, which is more difficult to analyze and which may be attributable to absorption involving excitons corresponding to conduction band Landau quantum numbers $n = 1$ and 2 , is also observed.

The lowest energy peak shows a quadratic behavior at low magnetic fields and was followed down to zero magnetic field. The separation between fine structure components is related to the separation between exciton energy levels. The experimental separations agree with the separations predicted by the theory of Elliott and Loudon.²

The variation with temperature of the zero field position of the absorption peak corresponding to the creation of an exciton in the ground state was studied. The position of the peak is constant within ± 0.1 meV between 4° and 18°K . It is reasonable to conclude that both the energy gap ϵ_g and the exciton binding energy R are constant in this range of temperature. Analysis of the exciton fine structure at $\sim 16^\circ\text{K}$ yields preliminary values of $\epsilon_g = 890.1$ meV and $R = 2.2$ meV.

A preliminary estimate gives a value of 9 kG for the magnetic field where $R = 1/2\hbar\omega_c$. Detailed spectra are observed for magnetic fields much smaller than 9 kG. This is the first detailed observation of the low field exciton region for a material with the diamond structure. The data provide a means of connecting the exciton energy levels in the low field region to those in the high field Landau level region.

E. J. Johnson

2. Far-Infrared Cyclotron Resonance in InSb

The cyanide gas laser has been used to observe cyclotron resonance of free carriers in the conduction band of InSb at wavelengths of 337, 311 (HCN) and 195 μ (DCN). Detection was accomplished through changes in photoconductivity of the sample which was modulated by the incident, chopped radiation. The requisite magnetic field was supplied by means of a superconducting solenoid (applied perpendicular to the sample surface and along the direction of light propagation). At each frequency a cyclotron resonance peak was obtained at 4.2°K as a function of magnetic field. The calculated effective masses are as follows: 337 μ , $m^* = 0.0138 m_0$; 311 μ , $m^* = 0.0139 m_0$; 195 μ , $m^* = 0.0143 m_0$. The dependence of mass on frequency (or magnetic field) is of course expected due to the nonparabolicity of the energy bands in InSb. The material was pure, intrinsic n-type InSb with an estimated carrier concentration of 5×10^{13} per cm^3 .

Section IV

The sample as well as the magnet and dewar were kindly loaned by C. Shivanandan of the Naval Research Laboratory, Washington, D.C.

At each wavelength a second absorption peak was observed on the low field side of cyclotron resonance. This absorption is associated with transitions between hydrogenic donor impurities. Preliminary qualitative analysis shows that the relative heights of the two types of peaks and their splittings as a function of temperature and wavelength are in accord with previous theoretical descriptions of the magneto-optical absorption spectrum of hydrogen-like states of bound impurities in a magnetic field.

A sufficient number of relatively strong signal sources throughout the far infrared spectrum are now available to us, permitting detailed measurements of the magneto-optical absorption of InSb.

P. E. Tannenwald J. Waldman*
C. D. Parker

3. Microwave Absorption in $\text{Pb}_{1-x}\text{Sn}_x\text{Te}$

Preliminary measurements of the absorption of 70-GHz microwave radiation in $\text{Pb}_{1-x}\text{Sn}_x\text{Te}$ have been made as a function of magnetic field at 4.2°K. Samples of n-type $\text{Pb}_{0.87}\text{Sn}_{0.13}\text{Te}$ and of p-type $\text{Pb}_{0.83}\text{Sn}_{0.17}\text{Te}$ and $\text{Pb}_{0.80}\text{Sn}_{0.20}\text{Te}$ have been placed in a resonant TE_{113} cavity in the Azbel-Kaner geometry (static magnetic field and microwave electric field parallel to the sample surface).

Two distinct effects have been observed: (1) Magneto-plasma cyclotron resonance, similar to that seen in PbTe ,³ PbSe ⁴ and Bi ,⁵ occurs at low magnetic fields, $\lesssim 3$ kG. As in these other materials,^{3,4,5} a fitting of the experimental curves with the classical skin effect theory for oriented samples yields values of the effective masses. (2) Shubnikov-deHaas oscillations are seen at fields usually above 3 kG. In particular, p-type $\text{Pb}_{0.83}\text{Sn}_{0.17}\text{Te}$ oriented with the microwave electric field, and the static magnetic field parallel to the [100] direction, exhibits oscillations in the absorption which are periodic in $1/H$, with a period of approximately 0.3×10^{-4} gauss⁻¹. By repeating the experiment at 35 GHz these oscillations have been verified to be independent of the frequency, and so can be distinguished from those due to cyclotron resonance which move to lower fields at the lower frequency.

In these experiments the derivative of the microwave power has been measured by the usual field modulation technique. In addition, the direct absorption has been measured by piezo-modulation, where the sample is attached to a ceramic transducer and the signal is detected at the vibration frequency of the transducer.

J. Melngailis T. C. Harman
W. C. Kernan J. O. Dimmock
J. G. Mavroides

4. Optical Studies in Bismuth-Doped Silicon

Measurements of the effect of stress on the transition from the ground 1s-like level of bismuth atoms in silicon to the spin-orbit split T_2 level,^{6,7} are being made. The measurements are made at low temperature on oriented samples of bismuth-doped silicon and with a longitudinal uniaxial stress of up to 6×10^8 dynes/cm². Similar measurements on sulfur in silicon have been reported earlier.⁸

*Physics Dept., M.I.T.

Calculations were made based on the assumption that the transitions are correctly identified as $1s(A_1) \rightarrow 1s(T_2)$ transitions, where the T_2 level (T_d symmetry) is split by spin-orbit coupling, and the form of the strain Hamiltonian is derived from effective mass and deformation potential theory. The energy shift of the various levels in units of the spin-orbit splitting Δ_{so} is given as a function of the strain parameter

$$u = \frac{(n_z^2 - \frac{1}{3}) E_2 (s_{11} - s_{12}) T}{\Delta_{so}} \quad (1)$$

where n_z is the component of the unit vector of the applied stress along the $[001]$ crystal axis, s_{11} and s_{12} are the usual strain coefficients, T is the applied stress (negative for compression) and E_2 is a pure shear deformation potential coefficient.

The experimental results are shown in Fig. IV-1 as points and the calculated curves as lines. The dashed lines were calculated using the value $E_2 = 7.9$ eV previously measured for the conduction band edge for sulfur in silicon⁸ and phosphorous in silicon.⁹ A better fit to this data is obtained with a value 10 percent lower ($E_2 = 7.1$ eV), although no attempt has yet been made to find the optimum fit.

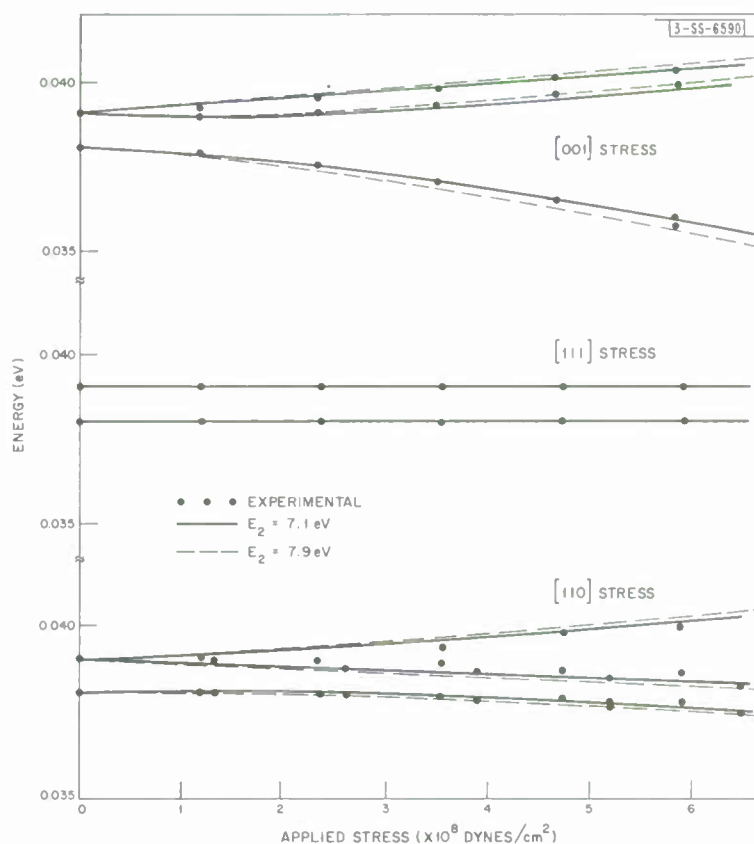


Fig. IV-1. Absorption peak position vs applied stress for transitions from $1s(A_1)$ ground state to spin-orbit split $1s(T_2)$ states in bismuth-doped silicon for stress applied along the three major crystal axes.

A study of the absorption intensity of these transitions as a function of the polarization of the light and the stress orientation is being carried out.

W. E. Krag
W. H. Kleiner
H. J. Zeiger

5. Γ_8 Dispersion Relations for HgTe and HgSe

Although the theoretical forms of the Γ_8 dispersion relations, $\epsilon(k)$, for the zincblende lattice were worked out by Dresselhaus¹⁰ and Parmenter¹¹ many years ago, the applicability of this work to the problem of the form of the band extrema in materials such as HgTe and HgSe has not been generally appreciated. This is in part due to the fact that simple analytic expressions for $\epsilon(k)$ can be found only for \vec{k} along [100] and [111] directions. For other directions the results are in the form of a 4×4 $\vec{k} \cdot \vec{p}$ interaction Hamiltonian,¹⁰ corresponding to the four Γ_8 bands. The $\vec{k} \cdot \vec{p}$ interactions of the Γ_8 bands with other bands to order k^2 are included as coefficients in the 4×4 matrix. Although some of these are not accurately known for HgTe, for example, it seems worthwhile to make reasonable guesses of their size and to numerically find the eigenvalues of the matrix Hamiltonian. This serves to point out both the applicability of the earlier theoretical work and to translate the results from matrix to graphical form for the case of a zincblende material with Γ_8 valence and conduction band extrema.

Following the work of Dresselhaus and Dresselhaus¹² we write the matrix Hamiltonian as a sum of an even part, $D^+(4)$, and an odd part, $D^-(4)$. For a material, such as Ge or α -Sn, with the diamond lattice, $D^-(4)$ is zero. $D^+(4)$ gives two twofold degenerate bands which are parabolic, but, in general, warped or fluted. In the 4×4 matrix treatment the Γ_6 band is treated as a "far away" band. This is a poor approximation for HgTe, with $\epsilon(\Gamma_8) - \epsilon(\Gamma_6) = 0.3 \text{ eV}$, for all but a small region of k -space near $\vec{k} = 0$. However, it is just this region which is of interest here. $D^-(4)$ is nonzero for zincblende materials and causes a splitting of the two-fold degeneracy at $\epsilon(\vec{k})$. (Time reversal symmetry gives the degeneracy of $\epsilon(\vec{k}) \uparrow$ with $\epsilon(-\vec{k}) \downarrow$, where \uparrow and \downarrow represent spin states.) An additional requirement for the presence of the $D^-(4)$ or splitting term is that the spin-orbit interaction be nonzero. The dissimilar basis-atoms of the zincblende lattice give rise to an antisymmetric potential which is felt by the electron orbits, and through the spin-orbit interaction, the spin degeneracy at a given \vec{k} is split.

Luttinger¹³ has written $D^+(4)$ in the general form

$$\begin{aligned} D^+(4) = & -(\hbar^2/2m)(\gamma_1 + 5/2 \gamma_2) k^2 + (\hbar^2/m) \gamma_2 (k_x^2 J_x^2 \\ & + k_y^2 J_y^2 + k_z^2 J_z^2) + (\hbar^2/m) \gamma_3 [k_x k_y (J_x J_y) \\ & + k_y k_z (J_y J_z) + k_x k_z (J_x J_z)] \end{aligned} \quad (2)$$

where $(J_x J_y) \equiv J_x J_y + J_y J_x$ and m is the free electron mass. The J_i are angular momentum matrices for $J = 3/2$, but with the matrix representations left unspecified. γ_1 , γ_2 and γ_3 are effective mass parameters which give the interaction of the Γ_8 bands with other bands. $D^-(4)$ has been given in specific form,¹⁰ and in general form.¹² The general form is:

$$D^-(4) = -\frac{C}{\sqrt{3}} \{k_x [J_x, (J_y^2 - J_z^2)] + k_y [J_y, (J_z^2 - J_x^2)] + k_z [J_z, (J_x^2 - J_y^2)]\} \quad (3)$$

The contributions to the parameter C have been discussed by Dresselhaus¹⁰ and by Kane.¹⁴

For the computer diagonalization of $D^+(4) + D^-(4)$, a representation with J_3 diagonal has been used and the k 's have been expressed in spherical coordinates. From a magnetoreflexion study¹⁵ on HgTe we found a reasonable set of higher band parameters to be

$$\bar{\gamma}_1 = 3.0, \quad \bar{\gamma}_2 = -0.5 \quad \text{and} \quad \bar{\gamma}_3 = 0.67 \quad (4)$$

where these numbers represent the interaction of Γ_8 with higher bands but not Γ_6 . For this problem the Γ_6 interaction is to be included. This can be done by writing

$$\gamma_1 = \bar{\gamma}_1 + \frac{\epsilon_P}{3E_G}, \quad \gamma_2 = \bar{\gamma}_2 + \frac{\epsilon_P}{6E_G} \quad \text{and} \quad \gamma_3 = \bar{\gamma}_3 + \frac{\epsilon_P}{6E_G} \quad (5)$$

where γ_1 , γ_2 and γ_3 are the parameters to be used in Eq. (2). With $\epsilon_G = -0.30$ eV and $\epsilon_P = 18$ eV,¹⁵ we find $\gamma_1 = -17.0$, $\gamma_2 = -10.5$ and $\gamma_3 = -9.33$.

The choice of C is more difficult. Robinson¹⁶ interprets a splitting of cyclotron resonance peaks in p-type InSb as due to the linear k terms. His estimate of the zincblende splitting corresponds to $C \approx 0.9 \times 10^{-9}$ eV-cm. A larger C for HgTe is expected because the greater ionicity of the crystal means a larger antisymmetric potential, while the spin-orbit splittings of HgTe and InSb are about the same. We have taken $C = 2 \times 10^{-9}$ eV-cm as a not unreasonable guess for HgTe. The maximum upbending of the valence band above the $k = 0$ value is proportional to C^2 , so our value of the upbending for HgTe is about five times larger than Robinson has estimated for InSb.

Figure IV-2 shows the dispersion curves for two directions which result from diagonalizing $D^+(4) + D^-(4)$. For \vec{k} along [100] directions, $D^-(4)$ contributes to the energy but does not split either the conduction or valence band. Both bands are split for \vec{k} along [110]. In the [111] directions, which are not shown, the conduction band is not split but the valence band splitting is maximum. The maximum upbending is 3.0×10^{-3} eV and occurs at $k = 2.2 \times 10^6$ cm⁻¹. This is about 1/20 of the distance from the origin to the closest point on the Brillouin zone boundary. The [111] directions are the only ones for which the conduction band and valence bands cross. For other directions the bands repel each other as shown for the [110] direction in Fig. IV-2.

The effect of the zincblende splitting on the Fermi surface is of interest for deHaas-vanAlphen (dHvA) or Shubnikov-deHaas (SdH) measurements. The conduction band splitting has been offered recently¹⁷ as an explanation of the beat frequencies in HgSe, observed by Whitsett. When the Fermi level is below the valence band maxima in the [111] directions, but above the upbending in the [110] directions, the valence band contribution to the Fermi surface is a set of eight ellipsoids, along the equivalent [111] directions; but when the Fermi level moves below the maximum upbending in the [110] direction, the ellipsoids connect. A multiply-connected valence band surface appropriate to the dashed line of Fig. IV-2 is shown in Fig. IV-3. Some evidence of the larger orbits on this type of surface have been seen in SdH measurements in very pure HgTe with fields up to 100 kG. However, we have lacked the orientable single crystals of this material needed to map out some of the features of the surface shown in Fig. IV-3.

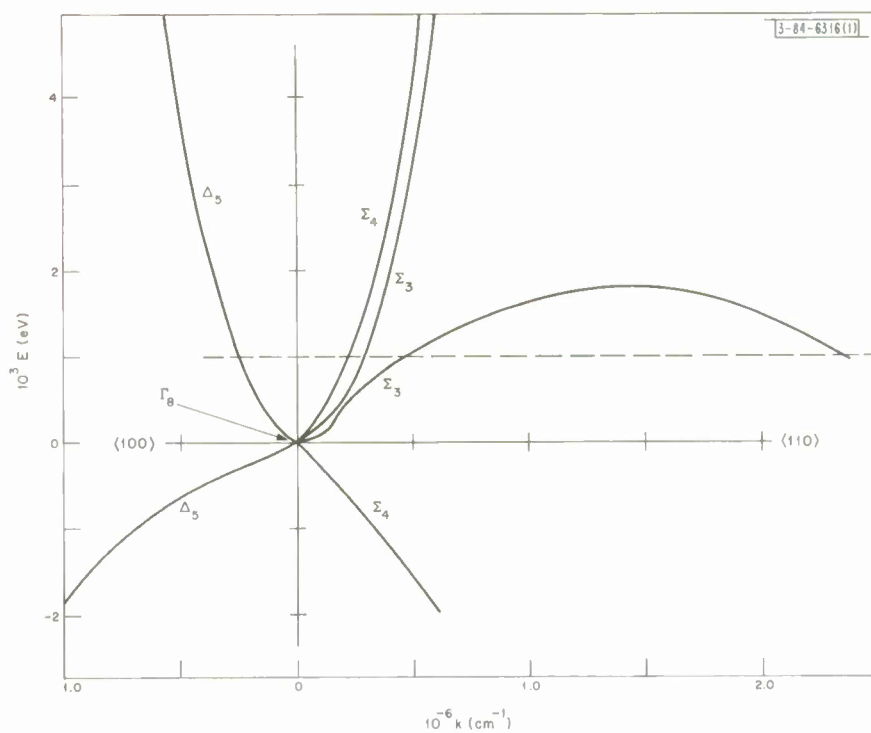


Fig. IV-2. Computed dispersion relations $E(\vec{k})$ for \vec{k} along $[100]$ and $[110]$ for top of valence band and bottom of conduction band in HgTe.

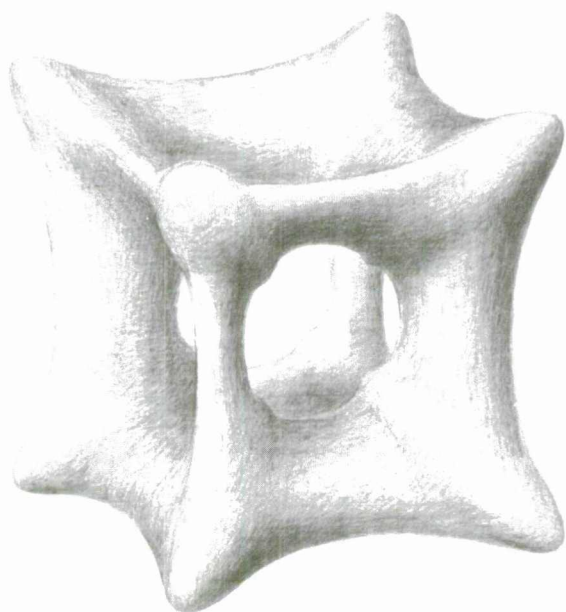


Fig. IV-3. Valence band contribution to Fermi surface at a Fermi energy corresponding to dashed line in Fig. IV-2.

In conclusion, this computational study graphically illustrates the difficulties of assuming simple band forms for materials like HgTe and HgSe, especially for the valence band of pure material. Secondly, the valence band Fermi surface for these materials, and for zincblende materials such as InSb as well, is interesting and our preliminary results indicate that it is experimentally feasible to do some mapping of this surface with the SdH measurements.

S. H. Groves

6. Some Properties of LCAO Bloch Functions (abstract of paper to be presented at APS Meeting at Berkeley in March 1968)

"Bloch sums $b_k(x)$ of atomic or localized orbitals $a(x)$ are calculated for two one-dimensional models, $a(x)$ being an exponential in one model, a Gaussian in the other. Closed form expressions are obtained for various physical quantities, and their properties are discussed in some detail. For example, for both models the localization of the charge density $|b_k(x)|^2$ increases as k increases from 0 to π ; $|b_0(x)|^2$ is less localized, and $|b_\pi(x)|^2$ is more localized than $\rho_c(x)$, the superposition of atomic charge densities. However, the total charge density $\rho(x)$ for a full band, proportional to the average of $|b_k(x)|^2$ over a Brillouin zone, is more localized than $\rho_c(x)$ whenever the nearest-neighbor overlap integral S is neither 0 nor 1. A particularly surprising result is that even as $S \rightarrow 1$, $\rho(x)$ is more localized than $\rho_c(x)$ (which approaches a constant) in the exponential case, whereas $\rho(x) \rightarrow \rho_c(x)$ in the Gaussian example. This type of result is shown to be valid for three-dimensional models as well. Other new properties of LCAO Bloch functions will also be discussed."

H. E. Stanley T. A. Kaplan
J. Hanus W. H. Kleiner

7. Effect of Orbital Overlap on Charge Densities in Crystals (abstract of paper to be presented at APS Meeting at Berkeley in March 1968)

"The Heitler-London approximation to the ground state of a crystal composed of closed-shell ions (e.g., MgO, LiH) is $\psi = \mathcal{Q} \prod_a D_a$, where D_a is a Slater determinant for ion a . The customarily-neglected effects of the antisymmetrizing operator \mathcal{Q} may well be important in interpreting measured charge densities. An effect of this "determinantal overlap" on the x-ray structure factor $f(q)$ can be illustrated for LiH, for example, by approximating the Li^+ and H^- one-electron wave functions by exponential 1s orbitals.¹⁸ We have calculated $f(q)$ for the rocksalt structure with two electrons per site, approximating the orbitals using Gaussian rather than exponential orbitals. We find that the ratio of $f(q)$ to the "conventional" (no overlap) structure factor $f_c(q)$ has a characteristic variation with q which is quite similar to that reported for an experiment on MgO.¹⁹ Moreover, a crude estimate of the actual magnitude of

Section IV



Fig. IV-4. Magnetic moment of high-pressure-phase MnAs as a function of temperature at several pressures between 4 and 9 kbars.

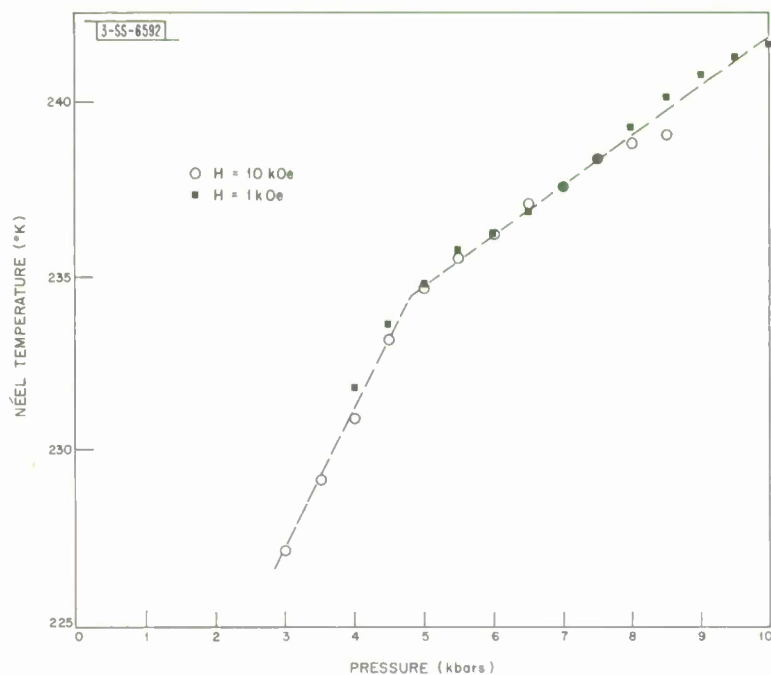


Fig. IV-5. Néel temperature of high-pressure-phase MnAs as a function of pressure in applied magnetic fields of 1 and 10 kOe.

this "overlap effect" for MgO shows that $f(q)$ can depart from $f_c(q)$ by roughly 5 percent, so that the effect should be experimentally significant."

T. A. Kaplan P. M. Raccah
J. Hanus H. E. Stanley
W. H. Kleiner

8. Effect of Orbital Overlap on Momentum Distributions in Crystals (abstract of paper to be presented at APS Meeting at Berkeley in March 1968)

"It has been pointed out²⁰ that for a filled band of LCAO Bloch functions, with overlap between the atomic orbitals neglected, the momentum distribution $\rho(p)$ is just the free atom momentum distribution. [$\rho(p)$ is of interest in connection with Compton effect and positron annihilation experiments.] We show that the change in $\rho(p)$ due to the overlap is first order in S for small S , where S is the nearest-neighbor overlap integral. This is to be compared with the corresponding change in the charge density (or, equivalently, the form factor) which is of order S^2 . This suggests that the effect of overlap on the momentum distribution is much greater than that on the charge density for "reasonable" values of S , and calculations on some simple models support this suggestion. The relation of our results to previous work will be discussed."

W. H. Kleiner T. A. Kaplan
J. Hanus H. E. Stanley

B. MAGNETISM

1. Magnetic Properties of High-Pressure-Phase MnAs

The study of the effects of pressure on the magnetic properties of MnAs has been continued. The problems which arose due to magnetic impurities contained in the original beryllium-copper pressure vessel were initially overcome by the use of an aluminum vessel to 6 kbars. Finally, a diamagnetic beryllium-copper alloy was obtained* and all measurements are now being performed in the pressure vessel made from this alloy.

With the MnAs sample in the high-pressure (B31) phase, measurements were made of the magnetization as a function of temperature at various pressures in a magnetic field of 10 kOe. The results are shown in Fig. IV-4.

The sharp local maxima observed in the curves in the temperature region 230° to 240°K are indicative of the onset of antiferromagnetic long range order. Taking the temperature of the local maximum as the Néel temperature T_N we have determined T_N as a function of pressure at 10 and 1 kOe. The results are shown in Fig. IV-5. The 1 kOe curve is limited on the low pressure end by the fact that in this field the maximum in the magnetic moments σ vs T curve is extremely shallow by 4 kbars, and below this pressure the onset of long range order is evidenced only by a change in slope of the σ vs T curve. Conversely, the 10 kOe curve is limited at the high pressure end of the curve by the large moment below T_N , as can be seen in Fig. IV-4.

* Beryllium-copper alloy 125 is manufactured by the Brush Beryllium Company. We have checked the diamagnetic behavior of our pressure vessel between 77° and 300°K.

Section IV

This effect tends to skew the local maximum, thereby reducing the apparent value of T_N at the higher pressures. Above 9 kbars in 10 kOe, the rising moment overtakes the local maximum. As seen in Fig. IV-5, the curve of pressure vs T_N consists of two approximately linear regions, as indicated by the dashed lines, with a relatively sharp bend between 4.5 and 5 kbars. Assuming linearity, we obtain $dT_N/dp = +4.0^\circ\text{K/kbar}$ for $p < 5$ kbars, and $dT_N/dp = +1.4^\circ\text{K/kbar}$ for $p > 5$ kbars. Grazhdankina and Bersenev²¹ also noted the presence of a Néel point in the high pressure phase of MnAs. Our results differ somewhat from the value $dT_N/dp = 2.3^\circ\text{K/kbar}$ which they reported on the basis of measurements made at pressures between approximately 4 and 9 kbars.

Were the sample to remain antiferromagnetic below T_N , the magnetic moment of the powder specimen at fixed field should decrease with decreasing temperature. Therefore, the subsequent increase in σ with decreasing temperature is indicative of either ferromagnetism or metamagnetism. Preliminary measurements of the field dependence at fixed temperature and pressure have been made at intermediate pressures (~ 5 to 6 kbars). These measurements did not indicate a ferromagnetic state. Further measurements of the magnetic field dependence of the moment at higher pressures are contemplated in order to definitively establish the magnetic state of the system.

It should be noted that our higher pressure curves in Fig. IV-4 are starting to resemble the magnetic moment vs temperature curve of MnP, which is isostructural with the high pressure phase of MnAs. MnP becomes ferromagnetic at 291.5°K , undergoes a transformation to the metamagnetic state at 50°K , and has an extrapolated 0°K moment of $1.29\mu_B$ /manganese ion.²² We intend to carry our σ vs T measurements to slightly higher pressures to further establish this similarity of behavior.

N. Menyuk K. Dwight
J. A. Kafalas J. B. Goodenough

2. Magnetic Resonance in Spiral Spin Structure Compounds

A calculation of the ground state ($T = 0^\circ\text{K}$) spin configuration for CoCr_2O_4 shows that a six-sublattice model is required rather than the previously considered three-sublattice model to minimize the energy. The resonance frequencies are in the process of being computed, using a six-sublattice model and taking into account the J_{AB} plus four J_{BB} exchange interactions. The dipole anisotropy contribution due to the spiral spin ordering has also been calculated for CoCr_2O_4 using the IBM-360 computer.

The ground state properties of a linear chain of two nonequivalent spins having near and next nearest neighbor J_{AB} and J_{BB} , respectively, exchange interactions, are being investigated. This model is the simplest one which is capable of describing a two-sublattice conical helix spin configuration. A study of the resonance modes for this idealized model should prove helpful in understanding the resonance behavior of more complicated conical spiral systems.

J. J. Stickler
H. J. Zeiger

3. Density Matrix Theory and Spin Wave Renormalization

Argyres and Kelley²³ have developed a decoupling procedure for obtaining reduced density matrix equations of motion for a system interacting with a bath and an external driving field.

The reduced density matrix equation of motion due to a driving interaction at angular frequency ω , to first order in the driving interaction, and second order in the interaction with the bath, can be written in Fourier transform form as

$$i\omega\rho_{ij}^S(\omega) = -i[\omega_{ij} + \omega_{ij}^{(1)}]\rho_{ij}^S(\omega) - \sum_{k,\ell} [\Gamma_{ijkl}^{(2)'}(\omega) + i\Gamma_{ijkl}^{(2)''}(\omega)]\rho_{kl}^S(\omega) \\ + \sum_{k,\ell,m} \bar{\Gamma}_{ijkl}^{(2)m}(\omega) \frac{\mathcal{H}_{kl}^S(\omega)}{\hbar(\omega + \omega_{kl})} \rho_{omm}^S - i \frac{\mathcal{H}_{ij}^S(\omega)}{\hbar} (\rho_{oii}^S - \rho_{ojj}^S) \quad (6)$$

In this equation, $\rho_{ij}^S(\omega)$ is the ω -Fourier component of the reduced density matrix of the system (defined as the density matrix of the entire system averaged over thermal bath variables). The quantity ω_{ij} is defined by

$$\omega_{ij} = \frac{\mathcal{H}_{Sii} - \mathcal{H}_{Sjj}}{\hbar} \quad (7)$$

where \mathcal{H}_S is the Hamiltonian of the system alone. $\omega_{ij}^{(1)}$ is the thermal average over bath variables of $(\mathcal{H}_{SB}/\hbar)_{ij}$, where \mathcal{H}_{SB} is the system-bath interaction. $\Gamma_{ijkl}^{(2)'}(\omega)$ is the real part of a sum of Fourier transforms of correlation functions $\langle \mathcal{H}_{SB}(\tau)\mathcal{H}_{SB}(0) \rangle$. $\omega_{ij}^{(1)}$ is first order in \mathcal{H}_{SB} ; and $\Gamma_{ijkl}^{(2)'}(\omega)$, $\Gamma_{ijkl}^{(2)''}(\omega)$ and $\bar{\Gamma}_{ijkl}^{(2)m}(\omega)$ are all second order in \mathcal{H}_{SB} . $\mathcal{H}_{kl}^S(\omega)$ is the ω -Fourier component of the driving perturbation. ρ_{omm}^S is the equilibrium reduced density matrix of the system, and therefore has only diagonal components. Equation (6) is something like a Bloch equation for the density matrix, and $\Gamma_{ijkl}^{(2)'}(\omega)$ is a frequency dependent relaxation matrix.

The term involving $\bar{\Gamma}_{ijkl}^{(2)m}(\omega)$ is called the interference term by Kelley and Argyres because it involves both system-bath relaxation effects and driving term effects. It represents the tendency of the system to relax toward instantaneous equilibrium, including the effect of the disturbance \mathcal{H}^S . This last term can be shown to be a generalization of the result of the Weisskopf-Van Vleck and Karplus-Schwinger treatments of relaxation toward instantaneous equilibrium (it approaches their results at high temperatures). It can also be shown, for a system of spin 1/2, to lead at high temperatures to the linearized Landau-Lifshitz or modified Bloch-Bloembergen equations of motion of spins in a magnetic field.

Equation (6) can also be used to obtain an expression for the contribution of a long wavelength spin wave to the susceptibility of a Heisenberg ferromagnet at low temperatures. To do this, the Heisenberg Hamiltonian is transformed by a Holstein-Primakoff transformation, followed by the introduction of spin wave variables,²⁴ to a Hamiltonian $\mathcal{H} = \mathcal{H}_0 + \mathcal{H}_1$. Here \mathcal{H}_0 is the usual decoupled spin-wave Hamiltonian involving Boson operators, and \mathcal{H}_1 represents the spin-wave interactions. If we interpret the spin-wave term in \mathcal{H}_0 for one particular spin wave of wavevector \vec{k} as the system, and all other spin-wave terms in \mathcal{H}_0 as the bath, then \mathcal{H}_1 represents \mathcal{H}_{SB} , the system-bath interaction. When the terms in Eq. (6) due to \mathcal{H}_{SB} are evaluated, it is found that the well known low temperature spin-wave renormalization term, which varies as $T^{5/2}$, comes from $\omega_{ij}^{(1)}$. The spin-wave damping result of Dyson²⁵ is contained in $\Gamma_{ijkl}^{(2)'}(\omega)$, and $\Gamma_{ijkl}^{(2)''}(\omega)$ represents a second-order spin-wave renormalization effect. It is then possible to write an expression for the susceptibility at low temperatures due to spin waves, in a form

which is the same as the low temperature limit of a result obtained by Marshall and Murray²⁶ using Green's function techniques.

H. J. Zeiger

4. A Vector Model for Arbitrary-Dimensional Spins: Exact Solution for Linear Chain and Bethe Lattice

Consider an open linear chain of $N + 1$ ν -dimensional vectors or "classical spins" \vec{S}_i of magnitude $\sqrt{\nu}$ and interacting isotropically via the Hamiltonian

$$\mathcal{H}^{(\nu)} = -2J \sum_{i=1}^N \vec{S}_i \cdot \vec{S}_{i-1} \quad (8)$$

where $-2J\nu$ is the interaction energy of a pair of nearest-neighbor spins on sites i and $i-1$. Solving exactly for the partition function and correlation function of $\mathcal{H}^{(\nu)}$, we can then obtain the energy, specific heat, and susceptibility.

We represent the constraint that each spin \vec{S}_i have magnitude $\sqrt{\nu}$ by the introduction of $N + 1$ δ -functions $\delta\left[\nu - \sum_{n=1}^{\nu} \sigma_n^2(i)\right]$, where the $\sigma_n(i)$ are the Cartesian coordinates of \vec{S}_i . Hence the partition function is

$$Q_N = A_N^{-1} \int \dots \int d\vec{S}_0 \dots d\vec{S}_N \prod_{i=0}^N \delta\left[\nu - \sum_{n=1}^{\nu} \sigma_n^2(i)\right] e^{-\beta \mathcal{H}^{(\nu)}} \quad (9)$$

where the normalization factor A_N is

$$A_N = \int \dots \int d\vec{S}_0 \dots d\vec{S}_N \prod_{i=0}^N \delta\left[\nu - \sum_{n=1}^{\nu} \sigma_n^2(i)\right] \quad (10)$$

The $(N + 1)$ -fold integral in the numerator of Eq. (9) factorizes into a product of integrals of the form

$$Z_i(x) = \int_{-\infty}^{\infty} \dots \int_{-\infty}^{\infty} d\sigma_1 \dots d\sigma_{\nu} \delta\left[\nu - \sum_{n=1}^{\nu} \sigma_n^2\right] \exp\left(x \sum_{n=1}^{\nu} c_n \sigma_n\right) \quad (11)$$

where $x \equiv 2J/kT$; we have dropped the subscript i from the integrand of Eq. (11) and have denoted $\sigma_n(i-1)$ by c_n since it is constant over the entire range of integration. Next we introduce the integral representation of the δ -function and obtain

$$Z_i(x) = \frac{x}{2\pi i} \int_{-i\infty}^{i\infty} d\alpha e^{\alpha \nu x} \prod_{n=1}^{\nu} \int_{-\infty}^{\infty} d\sigma_n \exp[x(-\alpha \sigma_n^2 + c_n \sigma_n)] \quad (12)$$

On completing the square, the integral on σ_n is found to be $(\pi/x\alpha)^{1/2} \exp[c_n^2 x/4\alpha]$, so that after using $\nu = \sum_{n=1}^{\nu} c_n^2$, we obtain

$$Z_1(x) = \frac{x}{2\pi i} (\pi/x)^{\nu/2} \int_{-i\infty}^{i\infty} d\alpha \exp[\nu x(\alpha + 1/\alpha)] \alpha^{-\nu/2} \quad (13)$$

Now on changing variables from α to $t \equiv 2\alpha$, we obtain an integral representation of the modified Bessel function of the first kind, and

$$Z_1(x) = \frac{x}{2} (2\pi/x)^{\nu/2} I_{\nu/2-1}(\nu x) \quad (14)$$

The normalization constant A_N is evaluated by the same method (with $x = 0$), and we finally obtain

$$Q_N = [(2/\nu x)^{\nu/2} \Gamma(\nu/2) I_{\nu/2-1}(\nu x)]^N \quad (15)$$

For $\nu = 1, 3$, and ∞ we obtain the known expressions for the Ising, Heisenberg and spherical models.

The spin correlation function $\langle \vec{S}_f \cdot \vec{S}_g \rangle$ is evaluated in exactly the same fashion, with the result

$$\langle \vec{S}_f \cdot \vec{S}_g \rangle = Y_\nu^R \quad (16)$$

where $R \equiv |\vec{f} - \vec{g}|$ is the distance between sites f and g , and

$$Y_\nu \equiv \begin{cases} I_{\nu/2}(\nu x)/I_{\nu/2-1}(\nu x) & \nu \text{ finite} \\ 2x/[1 + (1 + 4x^2)^{1/2}] & \nu = \infty \end{cases} \quad (17)$$

The internal energy per spin E is just proportional to the nearest-neighbor spin correlation function Y_ν ,

$$E = -2J\nu Y_\nu \quad (18)$$

and the specific heat is the temperature derivative of E . The reduced susceptibility $\bar{\chi} \equiv \chi/\chi_{\text{para}}$ may be obtained from the spin correlation function by using the fluctuation dissipation theorem, with the result

$$\bar{\chi} = \frac{1 + Y_\nu}{1 - Y_\nu} \quad (19)$$

For a Bethe lattice of coordination number z , the identical spin correlation function is obtained and the resulting susceptibility is

$$\bar{\chi} = \frac{1 + Y_\nu}{1 - (z-1) Y_\nu} \quad (20)$$

H. E. Stanley

5. Dependence of Critical Properties on Dimensionality of Spins (abstract of paper scheduled to appear in Phys. Rev. Letters)

"A new model Hamiltonian, $\mathcal{H}^{(\nu)} \equiv -2J \sum \langle i, j \rangle \vec{S}_i^{(\nu)} \cdot \vec{S}_j^{(\nu)}$, is introduced, where $\vec{S}_i^{(\nu)}$ are ν -dimensional classical "spins"; $\mathcal{H}^{(\nu)}$ reduces to the Ising, Vaks-Larkin, Heisenberg, and spherical models, respectively, for $\nu = 1, 2, 3$, and ∞ . Certain critical properties of $\mathcal{H}^{(\nu)}$ are found to be smooth functions of ν . In particular, the critical temperature $T_c^{(\nu)}$ for two-dimensional lattices decreases monotonically from its exact value for $\nu = 1$ to its exact value (zero) for $\nu = \infty$."

H. E. Stanley

C. LASER SCATTERING AND NONLINEAR EFFECTS

1. Stimulated Raman and Brillouin Scattering in Quartz

Two new features of stimulated Raman and Brillouin scattering in quartz have been observed. First a doublet spaced by 0.10 to 0.15 cm^{-1} has been obtained in the Raman spectrum of the " 128 " cm^{-1} E-mode of a z-cut sample at liquid helium temperature. Secondly, iterative backward-forward Brillouin shifts have been achieved directly in the sample without the usual laser reamplification process.

(a) Stimulated Raman Scattering

The Raman doublet can be attributed to the frequency difference for forward and backward scattering due to the coupling of the vibrational mode to the infrared. In the previous Solid State Research Report,²⁷ the splitting was calculated to be 0.19 cm^{-1} from an oscillator strength based on room temperature infrared absorption.²⁸ However, this absorption is known to decrease on lowering the temperature²⁹ leading to the smaller value observed for the splitting. Cavity modes of the 1.27-cm long crystal can be ruled out because they are spaced 0.26 cm^{-1} apart. The cavity however does play a role since the relative intensity of the two lines of the doublet is the same in the forward and backward monitors, as shown in Fig. IV-6(a).

-SS-6593

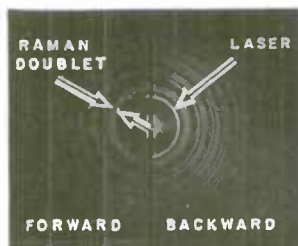
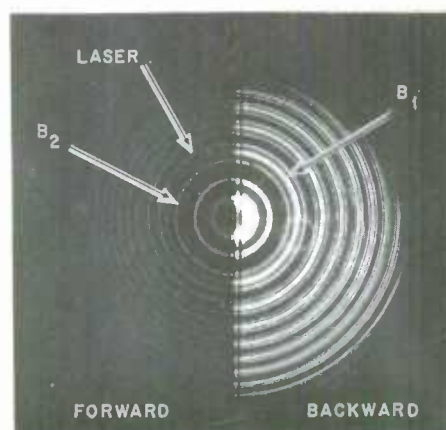


Fig. IV-6(a). Interferogram of stimulated Raman scattering from z-cut quartz at He temperature (etalon interorder spacing is 0.787 cm^{-1} ; laser is enhanced artificially in backward direction).

(b) Stimulated Brillouin Scattering

Figure IV-6(b) shows two iterative Brillouin shifts from an x-cut sample at room temperature monitored in the forward and backward directions. In the forward direction the first Stokes shift (B_1) is weaker than the second (B_2), contrary to the intensity pattern in the backward

Fig. IV-6(b). Interferogram of stimulated Brillouin scattering from x-cut quartz at room temperature (etalon interorder spacing is 3.15 cm^{-1}).



direction. This indicates that stimulation of B_2 arises directly from a back-traveling B_1 pump. Usually the B_1 wave is turned around and reamplified by the laser ruby, and higher order Stokes shifts are produced in the same manner as B_1 .³⁰ Such a process yields forward intensity patterns similar to the backward. The backward-forward iteration process of Fig. IV-6(b) occurs slightly above threshold; usually it is masked by the reamplification process when overdriven.

A. S. Pine
P. E. Tannenwald
F. H. Perry

2. Two-Phonon Infrared and Raman Spectrum of CdTe

The phonon spectrum of CdTe has been studied at 300° , 77° , and 4.2°K by far infrared absorption and Raman scattering. The Raman source was a YAG:Nd³⁺ laser operating at 1.06 microns with a continuous output power of several watts. The first order scattering from the zone center LO phonon at 171 cm^{-1} is at least an order of magnitude greater than that from the TO phonon at 140 cm^{-1} . From this fact, we conclude that the electro-optic contribution to the scattering tensor for the longitudinal mode is much greater than the deformation potential contribution. This is consistent with observations on other II-VI compounds, and in contrast to observations of III-V compounds. For samples where the conduction electron plasma frequency is comparable to the LO phonon frequency, the LO phonon was observed to broaden and shift to higher frequencies, which is indicative of the plasmon-LO phonon coupling.³¹ The scattering cross section of the LO phonon compared to that for GaAs is experimentally found to be consistent with a prediction based on the square of the ratio of their electro-optic coefficients as determined from direct optical measurements at a wavelength of 1μ . In the two-phonon spectrum, both sum and difference bands were observed, strongly activated at room temperature

Section IV

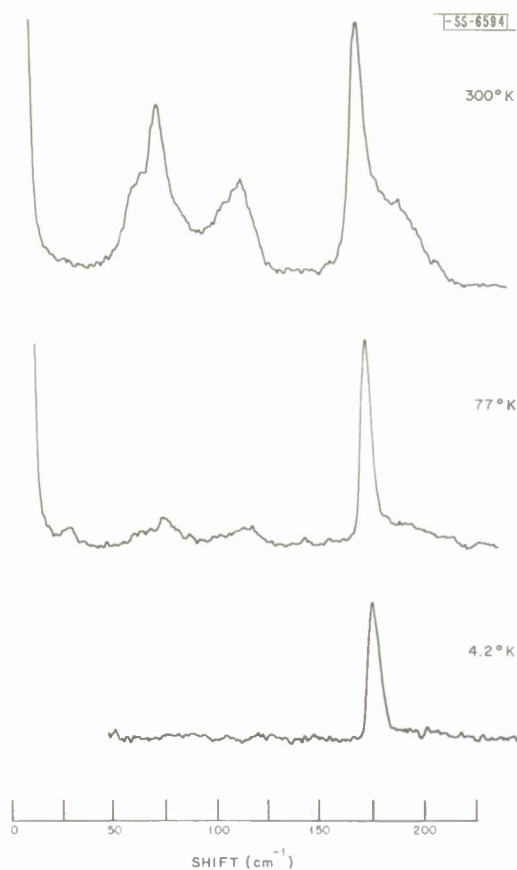


Fig. IV-7. First and second order spectrum of CdTe at 300°, 77° and 4.2°K.

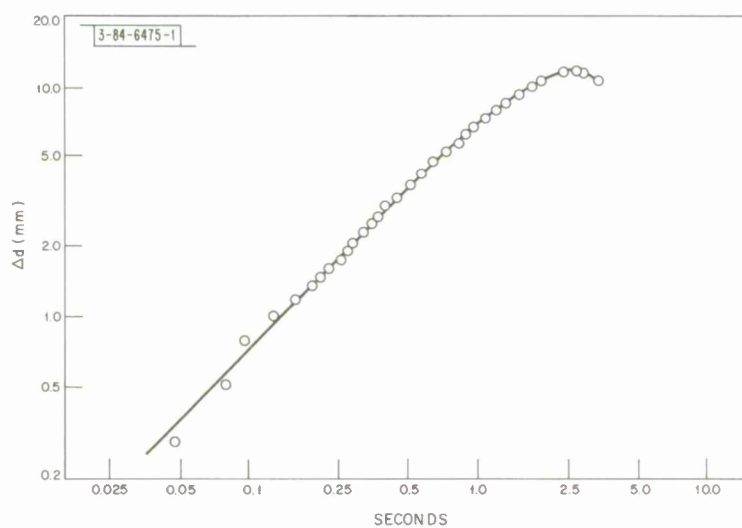


Fig. IV-8. Plot of change in beam diameter Δd vs time for a 38-cm cell of CCl_4 with enough dissolved iodine to produce $1/\alpha = 10.6$ cm.

as shown in Fig. IV-7. Raman scattering studies of the two-phonon spectrum, using polarized light and oriented single crystals, showed that the main contributions exhibited a diagonal scattering tensor, in contrast to the $\Gamma_{25'}$ symmetry found in silicon.³² Thus, for these lines we can exclude the decay of a virtual zone center phonon through the anharmonic phonon interaction as an important Raman process in CdTe. Assuming the approximate validity of the Brout sum rule, we obtain zone boundary phonon energies of $LO = 150 \text{ cm}^{-1}$, $TO = 139 \text{ cm}^{-1}$, $LA = 97 \text{ cm}^{-1}$ and $TA = 35 \text{ cm}^{-1}$.

A. Mooradian
G. B. Wright

3. Time Dependence in Thermal Defocusing

Continuing our earlier work,³³ the time dependence of thermal defocusing of a laser beam has been studied using the 4880 \AA CW argon laser line which passes through a liquid cell containing CCl_4 , with small amounts of dissolved iodine used as an absorber. The cell is followed by a diffusing screen upon which a 64-frame-per-second, 16-mm Cine Kodak Special motion picture camera was focused. Distance was calibrated by placing a scale on the screen. After development, the film was projected on a motion picture screen using a stop frame projector, and the beam diameter measured as a function of time. Under certain conditions³⁴ the beam is found to expand linearly with time t ; under others³⁵ it expands with a time dependence approaching $t^{1/2}$. The transition region corresponds to the experimental situation where the defocusing length $f \sim$ attenuation length $1/\alpha \sim$ cell length, ℓ .

Figure IV-8 shows the time dependence of the diameter change for $\ell = 38 \text{ cm}$, $1/\alpha = 10.6 \text{ cm}$, and the laser power = 72 mW. The diameter change has been normalized to that of a 1-meter cell for possible comparison with Fig. IV-9. The linear time dependence is characteristic of the conditions $1/\alpha \ll f, \ell$.

Figure IV-9 is a superposition of two runs with different film densities. The experimental conditions were $\ell = 100 \text{ cm}$, $1/\alpha = 90 \text{ cm}$, and laser power = 62 mW. These conditions lead

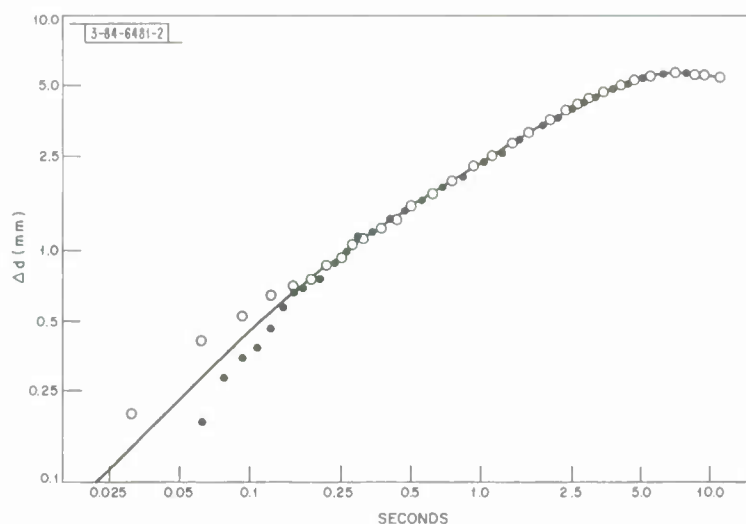


Fig. IV-9. Plot of change in beam diameter at end of cell Δd vs time for a 1-m cell of CCl_4 with enough dissolved iodine to produce $1/\alpha = 90 \text{ cm}$.

Section IV

to a smooth transition from $f \gg 1/\alpha$, ℓ which also shows a linear time dependence, to $f < 1/\alpha$, ℓ which causes the approach to $t^{1/2}$. The linear time dependence initially gradually changes and approaches $t^{1/2}$ before convection or conduction becomes significant. Since the condition $f \ll \ell$, $1/\alpha$ was never reached, neither was the $t^{1/2}$ dependence. The large initial scatter in the data was due in part to the required subtraction and in part to the high density of the image on the screen.

R. L. Carman
P. L. Kelcy

REFERENCES

1. E.J. Johnson, Phys. Rev. Letters 19, 352 (1967).
2. R.J. Elliott and R. Loudon, J. Phys. Chem. Solids 15, 196 (1959).
3. R. Nii, J. Phys. Soc. Japan 19, 58 (1964); H. Numata and Y. Uemura, J. Phys. Soc. Japan 19, 2140 (1964); M. Fujimoto, J. Phys. Soc. Japan 21, 1706 (1966).
4. S. Bermon, Phys. Rev. 158, 723 (1967).
5. G.E. Smith, L.C. Hebel, and S.J. Buchsbaum, Phys. Rev. 129, 154 (1963).
6. Solid State Research Report, Lincoln Laboratory, M.I.T. (1962:3), p. 23, DDC 291546.
7. W.E. Krag and H.J. Zeiger, Phys. Rev. Letters 8, 485 (1962).
8. W.E. Krag, W.H. Kleiner, H.J. Zeiger, and S. Fischler, Proceedings of the International Conference on the Physics of Semiconductors, Kyoto, 1966, J. Phys. Soc. Japan 21S, 230 (1966).
9. Solid State Research Report, Lincoln Laboratory, M.I.T. (1967:4) p. 31.
10. G. Dresselhaus, Phys. Rev. 100, 580 (1955).
11. R.H. Parmenter, Phys. Rev. 100, 573 (1955).
12. G. Dresselhaus and M.S. Dresselhaus, The Optical Properties of Solids, edited by J. Tauc (Academic Press, N.Y., 1966), p. 198.
13. J.M. Luttinger, Phys. Rev. 102, 1030 (1956).
14. E.O. Kane, in Semiconductors and Semimetals, edited by R.K. Willardson and A.C. Beer (Academic Press, New York, 1967), Vol. 1, "Physics of III-V Compounds."
15. S.H. Groves, R.N. Brown, and C.R. Pidgeon, Phys. Rev. 161, 779 (1967).
16. M. L.A. Robinson, Phys. Rev. Letters 17, 963 (1966).
17. L.M. Roth, S.H. Groves, and P.W. Wyatt, Phys. Rev. Letters 19, 576 (1967).
18. I. Waller and S.O. Lundqvist, Arkv. f. Fysik 7, 121 (1953).
19. P.M. Raccah and R.J. Arnett, Phys. Rev. 153, 1028 (1967).
20. S. Berko and J.S. Plaskett, Phys. Rev. 112, 1877 (1958).

21. N. P. Grazhdankina and Y. S. Bersenev, Soviet Phys. — JETP 24, 707 (1967).
22. E. E. Huber, Jr. and D. H. Ridgley, Phys. Rev. 135, A1033 (1964).
23. P. N. Argyres and P. L. Kelley, Phys. Rev. 134, A98 (1964).
24. T. Oguchi, Phys. Rev. 117, 117 (1960).
25. F. J. Dyson, Phys. Rev. 102, 1217 (1956).
26. W. Marshall and G. Murray (to be published in Proc. of Sept. 1967 International Congress on Magnetism held in Boston, Mass.)
27. Ref. 9, p. 45.
28. E. E. Russell and E. E. Bell, J. Opt. Soc. Am. 57, 341 (1967).
29. J. N. Plendl, L. C. Hansur, A. Hadni, F. Brehet, P. Henry, G. Morlot, F. Naudin, and P. Strimer, J. Phys. Chem. Solids 28, 1589 (1967).
30. E. M. Garmire and C. H. Townes, Appl. Phys. Letters 5, 84 (1964).
31. A. Mooradian and G. B. Wright, Phys. Rev. Letters 16, 999 (1966).
32. G. B. Wright and A. Mooradian, Phys. Rev. Letters 18, 608 (1967).
33. Ref. 9, p. 48.
34. J. P. Gordon, R. C. C. Leite, R. S. Moore, S. P. S. Porto, and J. R. Whinnery, J. Appl. Phys. 36, 3 (1965).
35. R. L. Carman and P. L. Kelley, unpublished.

DOCUMENT CONTROL DATA - R&D

(Security classification of title, body of abstract and indexing annotation must be entered when the overall report is classified)

1. ORIGINATING ACTIVITY (Corporate author) Lincoln Laboratory, M.I.T.		2a. REPORT SECURITY CLASSIFICATION Unclassified	
		2b. GROUP None	
3. REPORT TITLE Solid State Research			
4. DESCRIPTIVE NOTES (Type of report and inclusive dates) Quarterly Technical Summary - 1 November 1967 through 31 January 1968			
5. AUTHOR(S) (Last name, first name, initial) McWhorter, Alan H.			
6. REPORT DATE 15 February 1968		7a. TOTAL NO. OF PAGES 68	7b. NO. OF REFS 71
8a. CONTRACT OR GRANT NO. AF 19(628)-5167		9a. ORIGINATOR'S REPORT NUMBER(S) Solid State Research (1968:1)	
b. PROJECT NO. 649L		9b. OTHER REPORT NO(S) (Any other numbers that may be assigned this report) ESD-TR-68-17	
c.			
d.			
10. AVAILABILITY/LIMITATION NOTICES This document has been approved for public release and sale; its distribution is unlimited.			
11. SUPPLEMENTARY NOTES None		12. SPONSORING MILITARY ACTIVITY Air Force Systems Command, USAF	
13. ABSTRACT This report covers in detail the solid state research work at Lincoln Laboratory for the period 1 November 1967 through 31 January 1968. The topics covered are Solid State Device Research, Optical Techniques and Devices, Material Research, and Physics of Solids.			
14. KEY WORDS solid state devices ion implantation laser scattering magnetoabsorption optical techniques laser research infrared photovoltaic detectors and devices crystal growth magnetism magnetoreflexion materials research electronic band structure Raman scattering magneto-optical research			